

¹ **Searches for Supersymmetry using the α_T
² variable with the CMS detector at the LHC**

³ Darren Burton

⁴ Imperial College London
⁵ Department of Physics

⁶ A thesis submitted to Imperial College London
⁷ for the degree of Doctor of Philosophy

Abstract

10

Declaration

11

I, the author of this thesis, declare that the work presented within this
document to be my own. The work presented in Chapters 3.4.1, 4 and 5
is a result of the authors own work or that of which I have been a major
contributor unless explicitly stated otherwise, and is carried out within the
context of the Imperial College London and CERN SUSY groups, itself a
subsection of the greater CMS collaboration. All figures and studies taken
from external sources are referenced appropriately throughout this document.

18

Darren Burton

19

Acknowledgements

20

Of the many people who deserve thanks, some are particularly prominent....

Preface

Contents

23	List of Figures	viii
24	List of Tables	xii
25	1. Introduction	2
26	2. A Theoretical Overview	5
27	2.1. The Standard Model	5
28	2.1.1. Gauge Symmetries of the SM	7
29	2.1.2. The Electroweak Sector and Electroweak Symmetry Breaking	9
30	2.2. Motivation for Physics Beyond the Standard Model	13
31	2.3. Supersymmetry Overview	15
32	2.3.1. R-Parity	16
33	2.4. Experimental signatures of SUSY at the LHC	17
34	2.4.1. Simplified Models	18
35	3. The LHC and the CMS Detector	20
36	3.1. The LHC	20
37	3.2. The CMS detector	23
38	3.2.1. Detector Subsystems	23
39	3.2.2. Tracker	24
40	3.2.3. Electromagnetic Calorimeter	25
41	3.2.4. Hadronic Calorimeter	26
42	3.2.5. Muon Systems	28
43	3.3. Event Reconstruction and Object Definition	28
44	3.3.1. Jets	28
45	3.3.2. B-tagging	30
46	3.4. Triggering System	32
47	3.4.1. The Level-1 Trigger	34

48	3.4.2. L1 Trigger Jet Algorithm	35
49	3.4.3. Measuring L1 Jet Trigger Efficiencies	36
50	3.4.4. Effects of the L1 Jet Seed	38
51	3.4.5. Robustness of L1 Jet Performance against Pile-up	41
52	3.4.6. Summary	43
53	4. SUSY searches in Hadronic Final States	45
54	4.1. An introduction to the α_T search	46
55	4.1.1. The α_T variable	48
56	4.2. Search Strategy	50
57	4.2.1. Physics Objects	53
58	4.2.2. Event Selection	55
59	4.2.3. Control Sample Definition	57
60	4.3. Trigger Strategy	61
61	4.4. A method to determine MC yields with higher statistical precision	61
62	4.5. Systematic Uncertainties on Transfer Factors	61
63	4.6. Searches for Natural SUSY with B-tag templates.	61
64	5. Results	62
65	5.1. Statistical Interpretation	62
66	5.2. Interpretation in Simplified Signal Models	62
67	A. Miscellaneous	63
68	A.1. Noise Filters	63
69	A.2. Primary Vertices	64
70	B. L1 Jets	65
71	B.1. Jet matching efficiencies	65
72	B.2. Leading Jet Energy Resolution	66
73	B.3. Resolution for Energy Sum Quantities	69
74	Bibliography	75

⁷⁵ List of Figures

⁷⁶ 2.1.	One loop quantum corrections to the Higgs squared mass parameter m_h^2 due to a fermion.	⁷⁷ 14
⁷⁸ 2.2.	Two example simplified model decay chains.	⁷⁹ 19
⁸⁰ 3.1.	A top down layout of the LHC, with the position of the four main detectors labelled.	⁸¹ 21
⁸² 3.2.	The total integrated luminosity delivered to and collected by Compact Muon Solenoid (CMS) during the 2012 8 TeV pp runs	⁸³ 22
⁸³ 3.3.	A pictorial depiction of the CMS detector.	⁸⁴ 24
⁸⁴ 3.4.	Illustration of the CMS Electromagnetic CALorimeter (ECAL).	⁸⁵ 26
⁸⁵ 3.5.	Schematic of the CMS Hadronic CALorimeter (HCAL).	⁸⁶ 27
⁸⁶ 3.6.	Combined Secondary Vertex (CSV) algorithm discriminator values in enriched $t\bar{t}$ and inclusive multi jet samples	⁸⁷ 31
⁸⁸ 3.7.	Data/MC b-tag scale factors derived using the Combined Secondary Vertex Medium Working Point (CSVM) tagger.	⁸⁹ 32
⁹⁰ 3.8.	Data/MC mis-tag scale factors derived using the CSVM tagger.	⁹¹ 33
⁹¹ 3.9.	The CMS Level 1 Trigger (L1) Trigger system.	⁹² 34
⁹² 3.10.	Illustration of the Level-1 jet finding algorithm.	⁹³ 36
⁹³ 3.11.	L1 jet efficiency turn-on curves as a function of the offline CaloJet and PFJet E_T	⁹⁴ 38
⁹⁵ 3.12.	L1 jet efficiency turn-on curves as a function of the offline CaloJet E_T for the 2012 run period B and C.	⁹⁶ 39

97	3.13. Trigger cross section for the L1HTT150 trigger path.	40
98	3.14. L1 H_T efficiency turn-on curves as a function of the offline CaloJet H_T	41
99	3.15. L1 jet efficiency turn-on curves as a function of the leading offline E_T Calo	
100	(left) and PF (right) jet, for low, medium and high pile-up conditions.	42
101	3.16. Fit values from an Exponentially Modified Gaussian (EMG) function fitted	
102	to the resolution plots of leading Calo jet E_T measured as a function of	
103	$\frac{(L1\ E_T - \text{Offline}\ E_T)}{\text{Offline}\ E_T}$ for low, medium and high pile-up conditions.	43
104	3.17. Fit values from an EMG function fitted to the resolution plots of leading	
105	PF jet E_T measured as a function of $\frac{(L1\ E_T - \text{Offline}\ E_T)}{\text{Offline}\ E_T}$ for low, medium and	
106	high pile-up conditions.	44
107	4.1. Reconstructed offline H_T for 11.7fb^{-1} of data after a basic pre-selection.	48
108	4.2. The event topologies of background QCD dijet events (right) and a generic	
109	SUPERSYmmetry (SUSY) signature with genuine \cancel{E}_T (left).	48
110	4.3. The α_T distributions for the low 2-3 (left) and high ≥ 4 (right) jet	
111	multiplicities after a full analysis selection and shown for $H_T > 375$	50
112	4.4. Pictorial depiction of the analysis strategy employed by the α_T search to	
113	increase sensitivity to a wide spectra of SUSY models.	52
114	B.1. Leading jet matching efficiency as a function of the offline CaloJet E_T	65
115	B.2. Resolution plots of the leading offline Calo E_T measured as a function of	
116	$\frac{(L1\ E_T - \text{Offline}\ E_T)}{\text{Offline}\ E_T}$ for low (a), medium (b) and high (c) pile-up conditions.	67
117	B.3. Resolution plots of the leading off-line PF E_T measured as a function of	
118	$\frac{(L1\ E_T - \text{Offline}\ E_T)}{\text{Offline}\ E_T}$ for low (a), medium (b) and high (c) pile-up conditions.	69
119	B.4. $\sum E_T$ resolution parameters in bins of Calo $\sum E_T$ measured for the	
120	defined low, medium and high pile up conditions.	70
121	B.5. $\sum E_T$ resolution parameters in bins of PF $\sum E_T$ measured for the defined	
122	low, medium and high pile up conditions.	70
123	B.6. \cancel{E}_T resolution parameters in bins of Calo \cancel{E}_T measured for the defined	
124	low, medium and high pile up conditions.	71

125	B.7. \cancel{E}_T resolution parameters in bins of PF \cancel{E}_T measured for the defined low,	
126	medium and high pile up conditions.	71
127	B.8. H_T resolution parameters in bins of Calo H_T measured for the defined	
128	low, medium and high pile up conditions.	72
129	B.9. H_T resolution parameters in bins of PF H_T measured for the defined low,	
130	medium and high pile up conditions.	72
131	B.10. \cancel{H}_T resolution parameters in bins of \cancel{H}_T measured for the defined low,	
132	medium and high pile up conditions.	73
133	B.11. \cancel{H}_T resolution parameters in bins of PF \cancel{H}_T measured for the defined low,	
134	medium and high pile up conditions.	73

¹³⁵ List of Tables

¹³⁶	2.1. The fundamental particles of the Standard Model (SM), with spin, charge and mass displayed.	6
¹³⁷		
¹³⁸	3.1. Results of a cumulative EMG function fit to the turn-on curves for L1 single jet triggers in 2012 Run Period C.	38
¹³⁹		
¹⁴⁰	3.2. Results of a cumulative EMG function fit to the turn-on curves for L1 single jet triggers in the 2012 run period B and C.	39
¹⁴¹		
¹⁴²	3.3. Results of a cumulative EMG function fit to the turn-on curves for H_T in 2012 run period B and C.	40
¹⁴³		
¹⁴⁴	3.4. Results of a cumulative EMG function fit to the efficiency turn-on curves for L1 single jet triggers in the 2012 run period C, for low,medium and high pile-up conditions.	41
¹⁴⁵		
¹⁴⁶		
¹⁴⁷	3.5. Results of a cumulative EMG function fit to the efficiency turn-on curves for Level-1 single jet triggers in the 2012 run period C, for low,medium and high pile-up conditions.	42
¹⁴⁸		
¹⁴⁹		
¹⁵⁰	4.1. A summary of the Simplified Model Spectra (SMS) models interpreted in this analysis, involving both direct (D) and gluino-induced (G) production of squarks and their decays.	46
¹⁵¹		
¹⁵²		
¹⁵³	4.2. Jet Identification criteria for the “loose” CaloJet ID used with the analysis.	53
¹⁵⁴		
¹⁵⁵	4.3. Muon Identification criteria used within the analysis for selection/veto purposes in the muon control/signal selections.	54
¹⁵⁶		
¹⁵⁷	4.4. Photon Identification criteria used within the analysis for selection/veto purposes in the $\gamma +$ jets control/signal selections.	54

158	4.5. Electron Identification criteria used within the analysis for veto purposes.	55
159	4.6. Jet thresholds used in the three H_T regions of the analysis.	56
160	B.1. Results of a cumulative EMG function fit to the turn-on curves for the	
161	matching efficiency of the leading jet in an event to a Level-1 jet in run	
162	2012C and 2012B data.	66

¹⁶³

“The Universe is about 1,000,000 years old.”

— Matthew Kenzie, 1987-present : Discoverer of the Higgs Boson.

¹⁶⁴

Chapter 1.

¹⁶⁵ Introduction

¹⁶⁶ During the 20th century great advances have been made in our understanding of the
¹⁶⁷ universe, where it comes from, where it is going and what it is made of. The Standard
¹⁶⁸ Model (**SM**) first formulated in the 1960's is one of the crowning achievements in science's
¹⁶⁹ quest to explain the most fundamental processes and interactions that make up our
¹⁷⁰ universe. It has provided a highly successful explanation of a wide range of phenomena
¹⁷¹ in Particle Physics and has stood up to extensive experimental scrutiny [1].

¹⁷² Despite it's successes it is not a complete theory, with significant questions remaining
¹⁷³ unanswered. It describes only three of the four known forces with gravity not incorpo-
¹⁷⁴ rated within the framework of the **SM**. Cosmological experiments infer that just $\sim 4\%$
¹⁷⁵ of the observable universe exists as matter, with elusive "Dark Matter" accounting for a
¹⁷⁶ further $\sim 23\%$ [2]. However no particle predicted by the **SM** is able to account for it. At
¹⁷⁷ higher energy scales and small distances the (non-)unification of the fundamental forces
¹⁷⁸ point to problems with the **SM** at least at higher energies not yet probed experimentally.

¹⁷⁹ Many theories exist as extensions to the **SM** and predict a range of observables
¹⁸⁰ that can be detected at the Large Hadron Collider (**LHC**) of which SUperSYmmetry
¹⁸¹ (**SUSY**) is one such example. It predicts a new symmetry of nature in which all current
¹⁸² particles in the **SM** would have a corresponding supersymmetric partner. Common to
¹⁸³ most Supersymmetric theories is a stable, weakly interacting Lightest Supersymmetric
¹⁸⁴ Partner (**LSP**), which has the properties of a possible dark matter candidate. The **SM**
¹⁸⁵ and the main principles of Supersymmetric theories are outlined in Chapter 2, with
¹⁸⁶ emphasis on placed on how experimental signatures of **SUSY** may reveal themselves at
¹⁸⁷ the **LHC**.

188 The experimental goal of the **LHC** is to further test the framework of the **SM**,
189 exploring the TeV mass scale for the first time, and to seek a connection between the
190 particles produced in proton collisions and dark matter. The first new discovery by
191 this extraordinary machine was announced on the 4th of July 2012. The long-awaited
192 discovery was the culmination decades of experimental endeavours in the search for the
193 Higgs boson, providing an answer to the mechanism of electroweak symmetry breaking
194 within the **SM** [3][4].

195 This discovery was made possible through data taken by the two multi purpose
196 detectors (**CMS** and A Toroidal LHC ApparatuS (**ATLAS**)) located on the **LHC** ring.
197 An experimental description of the **CMS** detector and the **LHC** is described in Chapter 3,
198 including some of the object reconstruction used by **CMS** in searches for **SUSY** signatures.
199 The performance of the **CMS** Level-1 calorimeter trigger, benchmarked by the author is
200 also included within this chapter.

201 The analysis conducted by the author is detailed within Chapter 4. This chapter
202 contains a description of the search for evidence of the production of Supersymmetric
203 particles at the **LHC**. The main basis of the search centres around the kinematic
204 dimensionless α_T variable, which provides strong rejection of backgrounds with fake
205 missing energy signatures whilst maintaining good sensitivity to a variety of **SUSY**
206 topologies. The author's work as an integral part of the analysis group is documented in
207 detail, which has culminated in numerous publications over the past two years. The latest
208 of which was published in the European Physical Journal C (**EPJC**) [5] and contains the
209 results which are discussed within this and the sequential Chapter.

210 The author in particular has played a major role in the extension of the α_T analysis into
211 the additional b-tagged and jet multiplicity dimensions increasing the sensitivity of the
212 analysis to a range of **SUSY** topologies. Additionally the author has worked extensively
213 in both increasing the statistical precision of electroweak predictions measured from
214 simulation through analytical techniques, and the derivation of a data driven systematic
215 uncertainty through the establishment of closure tests within the control samples of the
216 analysis.

217 Also included within this Chapter is a method to search for **SUSY** signatures which
218 are rich in top and bottom flavoured jet final states. A parametrisation of the b-tagging
219 distribution for different Electroweak processes is used to establish templates, which
220 are then used to estimate the expected number of 3 or 4 b-tagged jet events from **SM**

221 processes. The α_T search is used as a cross check for this template method to establish
222 it's functionality.

223 Finally the interpretation of such results within the framework of a variety of Simplified
224 Model Spectra (**SMS**), which describe an array of possible **SUSY** event topologies is
225 documented in Chapter 5. A description of the statistical model used to derive these
226 interpretations and the possible implications of the results presented in this thesis is
227 discussed within this Chapter. Natural units are used throughout this thesis in which \hbar
228 = c = 1.

Chapter 2.

²²⁹ A Theoretical Overview

²³⁰ Within this chapter, a brief introduction and background to the **SM** is given. Its success
²³¹ as a rigorously tested and widely accepted theory is discussed as well as the deficiencies
²³² with this theory that hint there this theory is not a complete description of our universe.
²³³ The motivations for new physics at the TeV scale and in particular Supersymmetric
²³⁴ theories are outlined within Section (2.3), with the chapter concluding with how an
²³⁵ experimental signature of such theories can be produced and observed at the **LHC**,
²³⁶ Section (2.4).

²³⁷ 2.1. The Standard Model

²³⁸ The **SM** is the name given to the relativistic Quantum Field Theory (**QFT**), where
²³⁹ particles are represented as excitations of fields, which describes the interactions and
²⁴⁰ properties of all the known elementary particles [6][7][8][9]. It is a renormalisable field
²⁴¹ theory which contains three symmetries: $SU(3)$ for colour charge, $SU(2)$ for weak isospin
²⁴² and $U(1)$ relating to weak hyper charge, which require its Lagrangian \mathcal{L}_{SM} to be invariant
²⁴³ under local gauge transformation.

²⁴⁴ Within the **SM** theory, matter is composed of spin $\frac{1}{2}$ fermions, which interact with each
²⁴⁵ other via the exchange of spin-1 gauge bosons. A summary of the known fundamental
²⁴⁶ fermions and bosons is given in Table 2.1.

²⁴⁷ Fermions are separated into quarks and leptons of which only quarks interact with
²⁴⁸ the strong nuclear force. Quarks unlike leptons are not seen as free particles in nature,
²⁴⁹ but rather exist only within baryons, composed of three quarks with an overall integer

Particle	Symbol	Spin	Charge	Mass (GeV)
First Generation Fermions				
Electron Neutrino	ν_e	$\frac{1}{2}$	0	$< 2.2 \times 10^{-6}$
Electron	e	$\frac{1}{2}$	-1	0.51×10^{-3}
Up Quark	u	$\frac{1}{2}$	$\frac{2}{3}$	$2.3^{+0.7}_{-0.5} \times 10^{-3}$
Down Quark	d	$\frac{1}{2}$	$-\frac{1}{3}$	$4.8^{+0.7}_{-0.3} \times 10^{-3}$
Second Generation Fermions				
Muon Neutrino	ν_μ	$\frac{1}{2}$	0	-
Muon	μ	$\frac{1}{2}$	-1	1.05×10^{-3}
Charm Quark	c	$\frac{1}{2}$	$\frac{2}{3}$	1.275 ± 0.025
Strange Quark	s	$\frac{1}{2}$	$-\frac{1}{3}$	$95 \pm 5 \times 10^{-3}$
Third Generation Fermions				
Tau Neutrino	ν_τ	$\frac{1}{2}$	0	-
Tau	τ	$\frac{1}{2}$	-1	1.77
Top Quark	t	$\frac{1}{2}$	$\frac{2}{3}$	173.5 ± 0.8
Bottom Quark	b	$\frac{1}{2}$	$-\frac{1}{3}$	4.65 ± 0.03
Gauge Bosons				
Photon	γ	1	0	0
W Boson	W^\pm	1	± 1	80.385 ± 0.015
Z Boson	Z	1	0	91.187 ± 0.002
Gluons	g	1	0	0
Higgs Boson	H	0	0	125.3 ± 0.5 [4]

Table 2.1.: The fundamental particles of the SM, with spin, charge and mass displayed. Latest mass measurements taken from [1].

charge, and quark-anti-quark pairs called mesons. Both leptons and quarks are grouped into three generations which have the same properties, but with ascending mass in each subsequent generation.

The gauge bosons mediate the interactions between fermions. The field theories of Quantum Electro-Dynamics (QED) and Quantum Chromo-Dynamics (QCD), yield massless mediator bosons, the photon and eight coloured gluons which are consequences of the gauge invariance of those theories, detailed in Section (2.1.1).

The unification of the electromagnetic and weak-nuclear forces into the current Electroweak theory yield the weak gauge bosons, W^\pm and Z through the mixing of the associated gauge fields. The force carriers of this theory were experimentally detected by

260 the observation of weak neutral current, discovered in 1973 in the Gargamelle bubble
 261 chamber located at European Organization for Nuclear Research (**CERN**) [10], with the
 262 masses of and the weak gauge bosons measured by the UA1 and U2 experiments at the
 263 Super Proton Synchrotron (**SPS**) collider in 1983 [11][12].

264 2.1.1. Gauge Symmetries of the SM

265 Symmetries are of fundamental importance in the description of physical phenomena.
 266 Noether's theorem states that for a dynamical system, the consequence of any symmetry
 267 is an associated conserved quantity [13]. Invariance under translations, rotations, and
 268 Lorentz transformations in physical systems lead to conservation of momentum, energy
 269 and angular momentum.

270 In the **SM**, a quantum theory described by Lagrangian formalism, the weak, strong and
 271 electromagnetic interactions are described in terms of “gauge theories”. A gauge theory
 272 possesses invariance under a set of “local transformations”, which are transformations
 273 whose parameters are space-time dependent. The requirement of gauge invariance within
 274 the **SM** necessitates the introduction of force-mediating gauge bosons and interactions
 275 between fermions and the bosons themselves. Given the nature of the topics covered by
 276 this thesis, the formulation of Electroweak Sector (**EWK**) within the **SM** Lagrangian is
 277 reviewed within this section.

278 The simplest example of the application of the principle of local gauge invariance
 279 within the **SM** is in Quantum Electro-Dynamics (**QED**), the consequences of which
 280 require a massless photon field [14][15].

281 Starting from the free Dirac Lagrangian written as

$$\mathcal{L} = \bar{\psi}(i\gamma^\mu \partial_\mu - m)\psi, \quad (2.1)$$

282 where ψ represents a free non interacting fermionic field, with the matrices $\gamma^\mu, \mu \in$
 283 $0, 1, 2, 3$ defined by the anti commutator relationship $\gamma^\mu \gamma^\nu + \gamma^\nu \gamma^\mu = 2\eta^{\mu\nu} I_4$ where $\eta^{\mu\nu}$ is
 284 the flat space-time metric $(+, -, -, -)$ and I_4 is the 4×4 identity matrix.

285 Under a local U(1) abelian gauge transformation in which ψ transforms as:

$$\psi(x) \rightarrow \psi'(x) = e^{i\theta(x)}\psi(x) \quad \bar{\psi}(x) \rightarrow \bar{\psi}'(x) = e^{i\theta(x)}\bar{\psi}(x) \quad (2.2)$$

286 the kinetic term of the Lagrangian does not remain invariant, due to the partial
287 derivative interposed between the $\bar{\psi}$ and ψ yielding,

$$\partial_\mu \psi \rightarrow e^{i\theta(x)} \partial_\mu \psi + i e^{i\theta(x)} \psi \partial_\mu \theta. \quad (2.3)$$

288 To ensure that \mathcal{L} remains invariant, a modified derivative, D_μ , that transforms
289 covariantly under phase transformations is introduced. In doing this a vector field A_μ
290 with transformation properties that cancel out the unwanted term in (2.3) must also be
291 included,

$$D_\mu \equiv \partial_\mu - ieA_\mu, \quad A_\mu \rightarrow A_\mu + \frac{1}{e} \partial_\mu \theta. \quad (2.4)$$

292 Invariance of the Lagrangian is then achieved by replacing ∂_μ by D_μ :

$$\begin{aligned} \mathcal{L} &= i\bar{\psi}\gamma^\mu D_\mu \psi - m\bar{\psi}\psi \\ &= \bar{\psi}(i\gamma^\mu \partial_\mu - m)\psi + e\bar{\psi}\gamma^\mu \psi A_\mu \end{aligned} \quad (2.5)$$

293 An additional interaction term is now present in the Lagrangian, coupling the Dirac
294 particle to this vector field, which is interpreted as the photon in QED. To regard this
295 new field as the physical photon field, a term corresponding to its kinetic energy must be
296 added to the Lagrangian from Equation (2.5). Since this term must also be invariant
297 under the conditions of Equation (2.4), it is defined in the form $F_{\mu\nu} = \partial^\mu A^\nu - \partial^\nu A^\mu$.

298 This then leads to the Lagrangian of QED:

$$\mathcal{L}_{QED} = \underbrace{i\bar{\psi}\gamma^\mu\partial_\mu\psi - \frac{1}{4}F_{\mu\nu}F^{\mu\nu}}_{\text{kinetic term}} + \underbrace{m\bar{\psi}\psi}_{\text{mass term}} + \underbrace{e\bar{\psi}\gamma^\mu\psi A_\mu}_{\text{interaction term}} \quad (2.6)$$

299 Within the Lagrangian there remains no mass term of the form $m^2A_\mu A^\mu$, which is
300 prohibited by gauge invariance. This implies that the gauge particle, the photon, must
301 be massless.

302 2.1.2. The Electroweak Sector and Electroweak Symmetry 303 Breaking

304 The same application of gauge symmetry and the requirement of local gauge invariance
305 can be used to unify QED and the Weak force in the Electroweak Sector (EWK).
306 The nature of EWK interactions is encompassed within a Lagrangian invariant under
307 transformations of the group $SU(2)_L \times U(1)_Y$.

308 The weak interactions from experimental observation [16], are known to violate parity
309 and are therefore not symmetric under interchange of left and right helicity fermions.
310 Thus within the SM the left and right handed parts of these fermion fields are treated
311 separately. A fermion field is then split into two left and right handed chiral components,
312 $\psi = \psi_L + \psi_R$, where $\psi_{L/R} = (1 \pm \gamma^5)\psi$.

313 The $SU(2)_L$ group is the special unitary group of 2×2 matrices U satisfying $UU^\dagger = I$
314 and $\det(U) = 1$. It may be written in the form $U = e^{-i\omega_i T_i}$, with the generators of the
315 group $T_i = \frac{1}{2}\tau_i$ where τ_i , $i \in 1,2,3$ being the 2×2 Pauli matrices

$$\tau_1 = \begin{pmatrix} 0 & 1 \\ 1 & 0 \end{pmatrix} \quad \tau_2 = \begin{pmatrix} 0 & -i \\ i & 0 \end{pmatrix} \quad \tau_3 = \begin{pmatrix} 1 & 0 \\ 0 & -1 \end{pmatrix}, \quad (2.7)$$

316 which form a non Abelian group obeying the commutation relation $[T^a, T^b] \equiv$
317 $if^{abc}T^c \neq 0$. The gauge fields that accompany this group are represented by $\hat{W}_\mu =$
318 $(\hat{W}_\mu^1, \hat{W}_\mu^2, \hat{W}_\mu^3)$ and act only on the left handed component of the fermion field ψ_L .

³¹⁹ One additional generator Y which represents the hypercharge of the particle under
³²⁰ consideration is introduced through the $U(1)_Y$ group acting on both components of the
³²¹ fermion field, with an associated vector boson field \hat{B}_μ .

³²² The $SU(2)_L \times U(1)_Y$ transformations of the left and right handed components of ψ
³²³ are summarised by,

$$\begin{aligned}\chi_L &\rightarrow \chi'_L = e^{i\theta(x) \cdot T + i\theta(x)Y} \chi_L, \\ \psi_R &\rightarrow \psi'_R = e^{i\theta(x)Y} \psi_R,\end{aligned}\tag{2.8}$$

³²⁴ where the left handed fermions form isospin doubles χ_L and the right handed fermions
³²⁵ are isosinglets ψ_R . For the first generation of leptons and quarks this represents

$$\begin{aligned}\chi_L &= \begin{pmatrix} \nu_e \\ e \end{pmatrix}_L, & \begin{pmatrix} u \\ d \end{pmatrix}_L \\ \psi_R &= e_R, & u_R, d_R\end{aligned}\tag{2.9}$$

³²⁶ Imposing local gauge invariance within \mathcal{L}_{EWK} is once again achieved by modifying
³²⁷ the covariant derivative

$$D_\mu = \partial_\mu - \frac{ig}{2} \tau^i W_\mu^i - \frac{ig'}{2} Y B_\mu,\tag{2.10}$$

³²⁸ where g and g' are the coupling constant of the $SU(2)_L$ and $U(1)_Y$ groups respectively.
³²⁹ Taking the example of the first generation of fermions defined in Equation.(2.9), with input
³³⁰ hypercharge values of -1 and -2 for χ_L and e_R respectively, would lead to a Lagrangian
³³¹ \mathcal{L}_1 of the form,

$$\begin{aligned}\mathcal{L}_1 = &\bar{\chi}_L \gamma^\mu [i\partial_\mu - g \frac{1}{2} \tau \cdot W_\mu - g' (-\frac{1}{2}) B_\mu] \chi_L \\ &+ \bar{e}_R \gamma^\mu [i\partial_\mu - g' (-1) B_\mu] e_R - \frac{1}{4} W_{\mu\nu} \cdot W^{\mu\nu} - \frac{1}{4} B_{\mu\nu} B^{\mu\nu}.\end{aligned}\tag{2.11}$$

³³² As in **QED**, these additional gauge fields introduce field strength tensors $B_{\mu\nu}$ and
³³³ $W_{\mu\nu}$,

$$\hat{B}_{\mu\nu} = \partial_\mu \hat{B}_\nu - \partial_\nu \hat{B}_\mu \quad (2.12)$$

$$\hat{W}_{\mu\nu} = \partial_\mu \hat{W}_\nu - \partial_\nu \hat{W}_\mu - g \hat{W}_\mu \times \hat{W}_\nu \quad (2.13)$$

³³⁴ corresponding to the kinetic energy and self coupling of the W_μ fields and the kinetic
³³⁵ energy term of the B_μ field.

³³⁶ None of these gauge bosons are physical particles, and instead linear combinations of
³³⁷ these gauge bosons make up γ and the W and Z bosons, defined as

$$W^\pm = \frac{1}{\sqrt{2}} (W_\mu^1 \mp i W_\mu^2) \quad \begin{pmatrix} Z_\mu \\ A_\mu \end{pmatrix} = \begin{pmatrix} \cos\theta_W & -\sin\theta_W \\ \sin\theta_W & \cos\theta_W \end{pmatrix} \begin{pmatrix} W_\mu^3 \\ B_\mu \end{pmatrix} \quad (2.14)$$

³³⁸ where the mixing angle, $\theta_w = \tan^{-1} \frac{g'}{g}$, relates the coupling of the neutral weak and
³³⁹ electromagnetic interactions.

³⁴⁰ As in the case of the formulation of the **QED** Lagrangian there remains no mass term
³⁴¹ for the photon. However this is also the case for the W, Z and fermions in the Lagrangian,
³⁴² contrary to experimental measurement. Any explicit introduction of mass terms would
³⁴³ break the symmetry of the Lagrangian and instead mass terms can be introduced through
³⁴⁴ spontaneous breaking of the **EWK** symmetry via the Higgs mechanism.

³⁴⁵ The Higgs mechanism induces spontaneous symmetry breaking through the introduc-
³⁴⁶ tion of a complex scalar SU(2) doublet field ϕ which attains a non-zero Vacuum
³⁴⁷ Expectation Value (**VEV**) [17][18][19][20].

$$\phi = \begin{pmatrix} \phi^+ \\ \phi^0 \end{pmatrix} \quad \text{with} \quad \begin{aligned} \phi^+ &\equiv (\phi_1 + i\phi_2)/\sqrt{2} \\ \phi^0 &\equiv (\phi_3 + i\phi_4)/\sqrt{2} \end{aligned} \quad (2.15)$$

348 The Lagrangian defined in Equation (2.11) attains an additional term \mathcal{L}_{Higgs} of the
349 form

$$\mathcal{L}_{Higgs} = \overbrace{(D_\mu \phi)^\dagger (D^\mu \phi)}^{\text{kinetic}} - \overbrace{\mu^2 \phi^\dagger \phi - \lambda (\phi^\dagger \phi)^2}^{\text{potential } V(\phi)} \quad (\mu^2, \lambda) > 0 \in \mathbb{R},$$

$$\mathcal{L}_{SM} = \mathcal{L}_{EWK} + \mathcal{L}_{Higgs}, \quad (2.16)$$

350 where the covariant derivative D_μ is that defined in Equation (2.10). The last two
351 terms of \mathcal{L}_{Higgs} correspond to the Higgs potential, in which positive real positive values
352 of μ^2 and λ are required to ensure the generation of masses for the bosons and leptons.
353 The minimum of this potential is found at $\phi^\dagger \phi = \frac{1}{2}(\phi_1^2 + \phi_2^2 + \phi_3^2 + \phi_4^2) = \mu^2/\lambda = v^2$,
354 where v represents the **VEV**.

355 Defining the ground state of the ϕ field to be consistent with the $V(\phi)$ minimum, and
356 then expanding around a ground state chosen to maintain an unbroken electromagnetic
357 symmetry thus preserving a zero photon mass [21] leads to

$$\phi_0 = \sqrt{\frac{1}{2}} \begin{pmatrix} 0 \\ v \end{pmatrix}, \quad \phi(x) = e^{i\tau \cdot \theta(x)/v} \sqrt{\frac{1}{2}} \begin{pmatrix} 0 \\ v + h(x) \end{pmatrix}, \quad (2.17)$$

358 where the fluctuations from the vacuum ϕ_0 are parametrized in terms of four real
359 fields, $\theta_1, \theta_2, \theta_3$ and $h(x)$.

360 Choosing to gauge away the three massless Goldstone boson fields by setting $\theta(x)$ to
361 zero and substituting $\phi(x)$ back into kinetic term of \mathcal{L}_{Higgs} from Equation (2.16) leads to
362 mass terms for the W^\pm and Z bosons

$$(D_\mu \phi)^\dagger (D^\mu \phi) = \frac{1}{2}(\partial_\mu h)^2 + \frac{g^2 v^2}{2} W_\mu^+ W^{-\mu} + \frac{v^2 g^2}{8 \cos^2 \theta_w} Z_\mu Z^\mu + 0 A_\mu A^\mu, \quad (2.18)$$

363 where the relations between the physical and electroweak gauge fields from Equation
364 (2.14) are used. The W^\pm and Z bosons can then be determined to be

$$M_W = \frac{1}{2}gv \quad M_Z = \frac{1}{2} \frac{gv}{\cos \theta_w}. \quad (2.19)$$

365 This mechanism is also used to generate fermion masses by introducing a Yukawa
 366 coupling between the fermions and the ϕ field [22], with the coupling strength of a particle
 367 to the ϕ field governing its mass. Additionally a scalar boson h with mass $m_h = v\sqrt{\frac{\lambda}{2}}$, is
 368 also predicted as a result of this spontaneous symmetry breaking and became known as
 369 the Higgs boson. Its discovery by the CMS and ATLAS experiments in 2012 is concrete
 370 evidence to support this method of mass generation within the SM.

371 2.2. Motivation for Physics Beyond the Standard 372 Model

373 As has been described, the SM has proved to be a very successful theory, predicting the
 374 existence of the W^\pm and Z bosons and the top quark long before they were experimentally
 375 observed. However the theory does not accurately describe all observed phenomena and
 376 has some fundamental theoretical flaws that hint at the need for additional extensions to
 377 the current theory.

378 On a theoretical level, the SM is unable to incorporate the gravitational interactions
 379 of fundamental particles within the theory. Whilst at the electroweak energy scales the
 380 relative strength of gravity is negligible compared to the other three fundamental forces,
 381 at much higher energy scales $M_{planck} \sim 10^{18} GeV$ quantum gravitational effects become
 382 increasingly dominant. The failure to reconcile gravity within the SM, demonstrates that
 383 the SM must become invalid at some higher energy scale.

384 Some other deficiencies with the SM include the fact that the predicted rate of
 385 Charge-Parity violation does not account for the matter dominated universe which we
 386 inhabit, and the SM prediction of zero neutrino mass conflicts with the observation of
 387 neutrino flavour mixing, attributed to mixing between neutrino mass eigenstates [23][24].

388 Perhaps one of the most glaring gaps in the predictive power of the SM is that there
 389 exists no candidate to explain the cosmic dark matter observed in galactic structures
 390 through indirect techniques including gravitational lensing and measurement of the
 391 orbital velocity of stars in galactic edges. Any such candidate must be very weakly

392 interacting which must also be stable, owing to the lack of direct detection of the decay
393 products of such an process. Providing a dark matter candidate is of the prime goals
394 which be tackled by any Beyond Standard Model (**BSM**) physics model.

395 The recent discovery of the Higgs boson whilst a significant victory for the predictive
396 power of the **SM**, brings with it still unresolved questions. This issue is commonly
397 described as the “hierarchy problem”.

398 In the absence of new physics between the TeV and Planck scale, calculating beyond
399 tree-level contributions to the Higgs mass term given by its self interaction, result in
400 divergent terms that push the Higgs mass up to the planck mass M_{planck} .

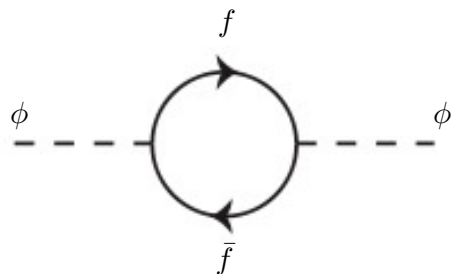


Figure 2.1.: One loop quantum corrections to the Higgs squared mass parameter m_h^2 due to a fermion.

401 This can be demonstrated by considering the one loop quantum correction to the
402 Higgs mass with a fermion f , shown in Figure 2.1 with mass m_f . The Higgs field couples
403 to f with a term in the Lagrangian $-\lambda_f h \bar{f} f$, yielding a correction of the form [25],

$$\delta m_h^2 = -\frac{|\lambda_f|^2}{8\pi^2} \Lambda^2 + \dots, \quad (2.20)$$

404 where λ_f represents the coupling strength for each type of fermion $\propto m_f$, and Λ the
405 cutoff energy scale at which the **SM** ceases to be a valid theory.

406 To recover the mass of the now discovered Higgs boson would require a fine-tuning of
407 the parameters to cancel out these mass corrections the the Higgs mass to the scale of
408 30 orders of magnitude. This appears as an unnatural solution to physicists and it is
409 this hierarchy problem that provides one of the strongest motivations for the theory of
410 SUperSYmmetry (**SUSY**).

⁴¹¹ 2.3. Supersymmetry Overview

⁴¹² Supersymmetry provides potential solutions to many of the issues raised in the previous
⁴¹³ section. It provides a dark matter candidate, can explain baryogenesis in the early
⁴¹⁴ universe and also provides an elegant solution to the hierarchy problem [26][27][28][29].
⁴¹⁵ At its heart it represents a new space-time symmetry that relates fermions and bosons.
⁴¹⁶ This symmetry converts bosonic states into fermionic states, and vice versa, see Equation
⁴¹⁷ (2.21) ,

$$Q|Boson\rangle = |Fermion\rangle \quad Q|Fermion\rangle = |Boson\rangle, \quad (2.21)$$

⁴¹⁸ where the operator Q is the generator of these transformations. Quantum field theories
⁴¹⁹ which are invariant under such transformations are called supersymmetric.

⁴²⁰ This symmetry operator therefore acts upon a particles spin altering it by a half integer
⁴²¹ value. The consequences of the introduction of this additional space-time symmetry
⁴²² introduce a new rich phenomenology. For example in supersymmetric theories, both
⁴²³ the left handed $SU(2)$ doublet and right handed singlet of fermions will have a spin-0
⁴²⁴ superpartner, containing the same electric charge, weak isospin, and colour as its **SM**
⁴²⁵ partner. In the case of the leptons $(\nu_l, l)_L$ will have two superpartners, a sneutrino $\tilde{\nu}_l{}_L$
⁴²⁶ and a slepton \tilde{l}_L , whilst the singlet l_R also has a superpartner slepton \tilde{l}_R .

⁴²⁷ Each particle in a supersymmetric theory is paired together with their superpartners
⁴²⁸ as a result of this supersymmetric transformations in a so called supermultiplet. These
⁴²⁹ superpartners will then consequently also contribute to the corrections to the Higgs mass.
⁴³⁰ Bosonic and fermionic loops contributing to the correction appear with opposite signs,
⁴³¹ and therefore cancellation of these divergent terms will stabilise the Higgs mass, solving
⁴³² the hierarchy problem [30][31].

⁴³³ One of the simplest forms of **SUSY** would predict a whole set of supersymmetric
⁴³⁴ partners to their **SM** counterparts with the same mass and interactions. However the
⁴³⁵ currently lack of any experimental evidence for the predicted sparticle spectrum implies
⁴³⁶ **SUSY** must be a broken symmetry in which any sparticle masses must be greater than
⁴³⁷ their SM counterparts.

⁴³⁸ There exist many techniques which can induce supersymmetric breaking [32][33][34].
⁴³⁹ Of particular interest to experimental physicists are those at which the breaking scale

⁴⁴⁰ is of an order that is experimentally accessible to the LHC i.e. \sim TeV scale. Whilst
⁴⁴¹ there is no requirement for supersymmetric breaking to occur at this energy scale, for
⁴⁴² supersymmetry to provide a solution to the hierarchy problem, it is necessary for this
⁴⁴³ scale to not differ too drastically from the EWK scale [35][36].

⁴⁴⁴ 2.3.1. R-Parity

⁴⁴⁵ Some supersymmetric theories also present a solution to the dark matter problem. Such
⁴⁴⁶ theories can contain a Lightest Supersymmetric Partner (LSP), which matches the criteria
⁴⁴⁷ of a Weakly Interacting Massive Particle (WIMP) required by cosmological observation
⁴⁴⁸ if R-parity is conserved.

⁴⁴⁹ Baryon (B) and Lepton (L) number conservation is forbidden in the SM by renor-
⁴⁵⁰ malisability requirements. The violation of Baryon or Lepton number would result in
⁴⁵¹ the proton lifetime much shorter than those set by experimental limits [37]. Another
⁴⁵² symmetry called R-parity is then often introduced to SUSY theories to maintain baryon
⁴⁵³ and lepton conservation.

⁴⁵⁴ R-parity is described by the equation

$$R_P = (-1)^{3(B-L)+2s}, \quad (2.22)$$

⁴⁵⁵ where s represents the spin of the particles. $B = \pm \frac{1}{3}$ for quarks/antiquarks and $B = 0$
⁴⁵⁶ for all others, $L = \pm 1$ for leptons/antileptons, $L = 0$ for all others.

⁴⁵⁷ R-parity ensures the stability of the proton in SUSY models, and also has other
⁴⁵⁸ consequences for the production and decay of supersymmetric particles. At particle
⁴⁵⁹ colliders supersymmetric particles can only be pair produced, and similarly the decay
⁴⁶⁰ of any produced supersymmetric particle is restricted to a SM particle and a lighter
⁴⁶¹ supersymmetric particle as allowed by conservation laws. A further implication of R-
⁴⁶² parity is that once a supersymmetric particle has decayed to the LSP it remains stable,
⁴⁶³ unable to decay into a SM particle.

⁴⁶⁴ A LSP would not interact in a detector at a particle collider, leaving behind a missing
⁴⁶⁵ energy \cancel{E}_T signature. The assumption of R-parity and its consequences are used to
⁴⁶⁶ determine the physical motivation and search strategies for SUSY model at the LHC.

467 2.4. Experimental signatures of SUSY at the LHC

468 Should strongly interacting sparticles be within the experimental reach of the LHC, then
469 it is expected that they can be produced in a variety of ways.

- 470 • squark/anti-squark and gluino pairs can be produced via both gluon fusion and
471 quark/anti-quark scattering.
- 472 • a gluino and squark produced together via quark-gluon scattering
- 473 • squark pairs produced via quark-quark scattering

474 Whilst most SUSY searches invoke the requirement of R-parity to explore parameter
475 phase space, there still exist a whole plethora of possible SUSY model topologies which
476 could be discovered at the LHC.

477 During the 2011 run period at a $\sqrt{s} = 7$ TeV particular models were used to benchmark
478 performance and experimental reach of both CMS searches and previous experiments.
479 The Compressed Minimal SuperSymmetric Model (CMSSM) was initially chosen for a
480 number of reasons [38]. One of the most compelling being the reduction from the up to
481 105 new parameters introduced by SUSY in addition to the existing 19 of the SM to that
482 of just 5 free extra free parameters. It was this simplicity, combined with the theory not
483 requiring any fine tuning of particle masses to produce the experimentally verified SM
484 that made it an attractive model to interpret physics results.

485 However recent results from the LHC now strongly disfavour large swathes of CMSSM
486 parameter space [39][40][41]. In the face of such results a more pragmatic model indepen-
487 dent search strategy is now applied across most SUSY searches at the LHC, see Section
488 (2.4.1).

489 As previously stated, a stable LSP that exhibits the properties of a dark matter would
490 be weakly interacting and therefore will not be directly detected in a detector environment.
491 Additionally the cascade decays of supersymmetric particles to the LSP would also result
492 in significant hadronic activity. These signatures can then be characterised through
493 large amounts of hadronic jets (see Section (3.3.1)), leptons and a significant amount of
494 missing energy dependent upon the size of the mass splitting between the LSP and the
495 supersymmetric particle it has decayed from.

496 Whilst the SM contains processes which can exhibit a similar event topology to that
497 described above. The largest contribution of which comes in from the general QCD

498 environment of a hadron collider. A multitude of different analytical techniques are used
 499 by experimental physicists to reduce or estimate any reducible or irreducible backgrounds,
 500 allowing a possible **SUSY** signature to be extracted. The techniques employed within
 501 this thesis are described in great detail within Section (4.1).

502 2.4.1. Simplified Models

503 With such a variety of different ways for a **SUSY** signal to manifest itself, it is necessary
 504 to be able to interpret experimental reach through the masses of gluinos and squarks
 505 which can excluded by experimental searches rather than on a model specific basis.

506 This is accomplished through **SMS** models, which are defined by a set of hypothetical
 507 particles and a sequence of their production and decay [42][43]. In the **SMS** models
 508 considered within this thesis, only the production process for the two primary particles
 509 are considered. Each primary particle can undergo a direct or a cascade decay through
 510 an intermediate new particle. At the end of each decay chain there remains a neutral,
 511 undetected **LSP** particle, denoted $\tilde{\chi}_{LSP}$ which can represent a neutralino or gravitino.
 512 Essentially it is easier to consider each **SMS** with branching ratios set to 100% The
 513 masses of the primary particle and the **LSP** remain as free parameters, in which the
 514 absolute value and relative difference between the primary and **LSP** particle alter the
 515 kinematics of the event.

516 Different **SMS** models are denoted with a T-prefix, with a summary of the types
 517 interpreted within this thesis listed below [44].

- 518 • **T1,T1xxxx**, models represent a simplified version of gluino pair production with
 519 each gluino (superpartner to the gluon) undergoing a three-body decay to a quark-
 520 antiquark pair and the **LSP** (i.e. $\tilde{g} \rightarrow q\bar{q}\tilde{\chi}_{LSP}$). The resultant final state from this
 521 decay is typically 4 jets + \cancel{E}_T in the absence of initial/final state radiation and
 522 detector effects. xxxx denotes models in which the quarks are of a specific flavour,
 523 typically t or b quark-antiquarks.
- 524 • **T2,T2xx**, models represent a simplified version of squark anti-squark production
 525 with each squark undergoing a two-body decay into a light-flavour quark and **LSP**
 526 (i.e. $\tilde{q} \rightarrow q\tilde{\chi}_{LSP}$). This results in final states with less jets than gluino mediated
 527 production, typically 2 jets + \cancel{E}_T when again ignoring the effect of initial/final state
 528 radiation and detector effects. xx models again represent decays in which both the
 529 quark and the squark within the decay is of a specific flavour, typically \tilde{t}/t or \tilde{b}/b .

Models rich in b and t quarks are interpreted within this thesis as they remain of particular interest within “Natural SUSY” scenarios [45][46]. The largest contribution to the quadratic divergence in the Higgs mass parameter comes from a loop of top quarks via the Yukawa coupling. Cancellation of these divergences can be achieved in supersymmetric theories by requiring a light right handed top squark, \tilde{t}_R , and left-handed double $SU(2)_L$ doublet containing top and bottom squarks, $(\tilde{\frac{t}{b}})_L$ [47].

These theories therefore solve the hierarchy problem by predicting light \sim EWK scale third generation sleptons, to be accessible at the LHC. Search strategies involving the requirement of b-tagging (see Section (3.3.2)) are used to give sensitivity to these type of SUSY scenarios and are discussed in greater detail within Chapter 5.

Two example decay chains are shown in Figure 2.2; the pair production of gluinos (T1) and the pair production of squarks (T2) decaying into SM particles and LSP’s.

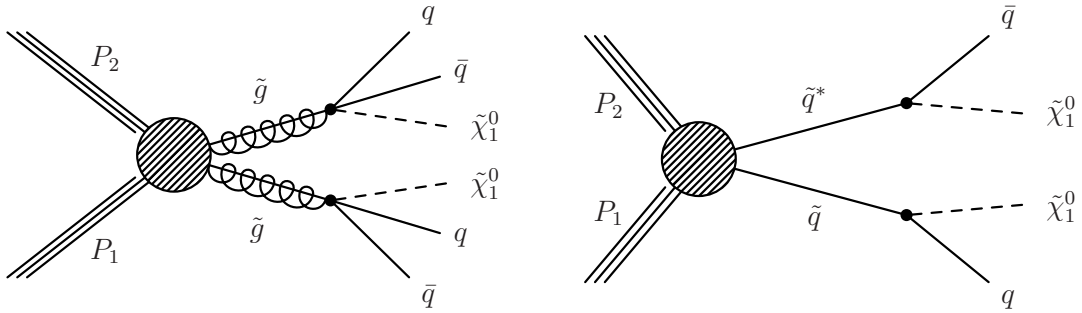


Figure 2.2.: Two example SMS model decays (T1 (left), T2 (right)), which are used in interpretations of physics reach by CMS.

Chapter 3.

⁵⁴² The LHC and the CMS Detector

⁵⁴³ Probing the SM for signs of new physics would not be possible without the immensely
⁵⁴⁴ complex electronics and machinery that makes the TeV energy scale accessible for the
⁵⁴⁵ first time. This chapter will cover the LHC based at European Organization for Nuclear
⁵⁴⁶ Research (CERN) and the Compact Muon Solenoid (CMS) detector, being the experiment
⁵⁴⁷ the author is a member of. Section (3.2) serves to introduce an overview of the different
⁵⁴⁸ components of the CMS detector, with more detail spent on those that are relevant in
⁵⁴⁹ the search for Supersymmetric particles. Section (3.3) will focus on event and object
⁵⁵⁰ reconstruction again with more emphasis on jet level quantities which are most relevant
⁵⁵¹ to the author's analysis research. Finally Section (3.4) will cover work performed by
⁵⁵² the author, as service to the CMS Collaboration, in measuring the performance of the
⁵⁵³ Global Calorimeter Trigger (GCT) component of the L1 trigger during the 2012-2013
⁵⁵⁴ run period.

⁵⁵⁵ 3.1. The LHC

⁵⁵⁶ The LHC is a storage ring, accelerator, and collider of circulating beams of protons or
⁵⁵⁷ ions. Housed in the tunnel dug for the Large Electron-Positron collider (LEP), it is
⁵⁵⁸ approximately 27 km in circumference, 100 m underground, and straddles the border
⁵⁵⁹ between France and Switzerland outside of Geneva. It is currently the only collider
⁵⁶⁰ in operation that is able to study physics at the TeV scale. A double-ring circular
⁵⁶¹ synchrotron, it was designed to collide both proton-proton (pp) and heavy ion (PbPb)
⁵⁶² with a centre of mass energy $\sqrt{s} = 14$ TeV at a final design luminosity of $10^{34}\text{cm}^{-2}\text{s}^{-1}$.

⁵⁶³

These counter-circulating beams of protons/Pb ions are merged in four sections around the ring to enable collisions of the beams, with each interaction point being home to one of the four major experiments; A Large Ion Collider Experiment (**ALICE**) [48], A Toroidal LHC ApparatuS (**ATLAS**) [49], Compact Muon Solenoid (**CMS**) [50] and Large Hadron Collider Beauty (**LHC-B**) [51] which record the resultant collisions. The layout of the **LHC** ring is shown in Figure 3.1. The remaining four sections contain acceleration, collimation and beam dump systems. In the eight arc sections, the beams are steered by magnetic fields of up to 8 T provided by super conduction dipole magnets, which are maintained at temperatures of 2 K using superfluid helium. Additional magnets for focusing and corrections are also present in straight sections within the arcs and near the interaction regions where the detectors are situated.

575

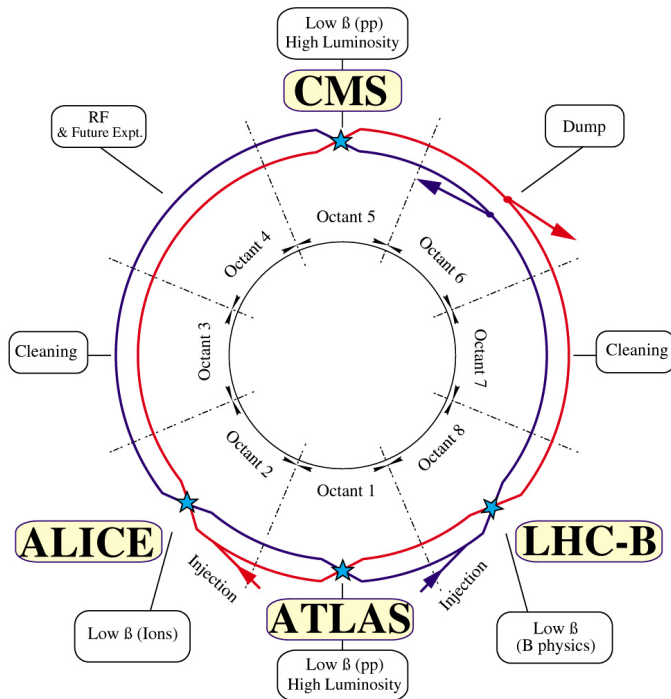


Figure 3.1.: A top down layout of the LHC. [52], with the position of the four main detectors labelled.

Proton beams are formed inside the Proton Synchrotron (**PS**) from bunches of protons 50 ns apart with an energy of 26 GeV. The protons are then accelerated in the Super Proton Synchrotron (**SPS**) to 450 GeV before being injected into the **LHC**. These **LHC** proton beams consists of many “bunches” i.e. approximately 1.1×10^{11} protons localized into less than 1 ns in the direction of motion. Before collision the beams are ramped to 4

576

581 TeV (2012) per beam in a process involving increasing the current passing through the
 582 dipole magnets. Once the desired \sqrt{s} energy is reached then the beams are allowed to
 583 collide at the interaction points. The luminosity falls regularly as the run progresses as
 584 protons are lost in collisions, and eventually the beam is dumped before repeating the
 585 process again.

586

587 Colliding the beams produced an instantaneous luminosity of approximately $5 \times$
 588 $10^{33} \text{ cm}^{-2}\text{s}^{-1}$ during the 2012 run. The high number of protons in each bunch increases
 589 the likelihood of multiple interactions with each crossing of the counter-circulating
 590 beams. This leads to isotropic energy depositions within the detectors positioned at these
 591 interaction points, increasing the energy scale of the underlying event. This is known as
 592 pile-up and the counteracting of it's effects are important to the many measurements
 593 performed at the **LHC**.

594 In the early phase of prolonged operation after the initial shutdown the machine
 595 operated in 2010-2011 at 3.5 TeV per beam, $\sqrt{s} = 7 \text{ TeV}$, delivering 6.13 fb^{-1} of data
 596 [53]. During the 2012-2013 run period, data was collected at an increased $\sqrt{s} = 8 \text{ TeV}$
 597 improving the sensitivity of searches for new physics. Over the whole run period 23.3
 598 fb^{-1} of data was delivered of which 21.8 fb^{-1} was recorded by the **CMS** detector as shown
 599 in Figure 3.2 [53]. A total of 12 fb^{-1} of 8 TeV certified data was collected by October
 600 2012, and it is this data which forms the basis of the results discussed within this thesis.

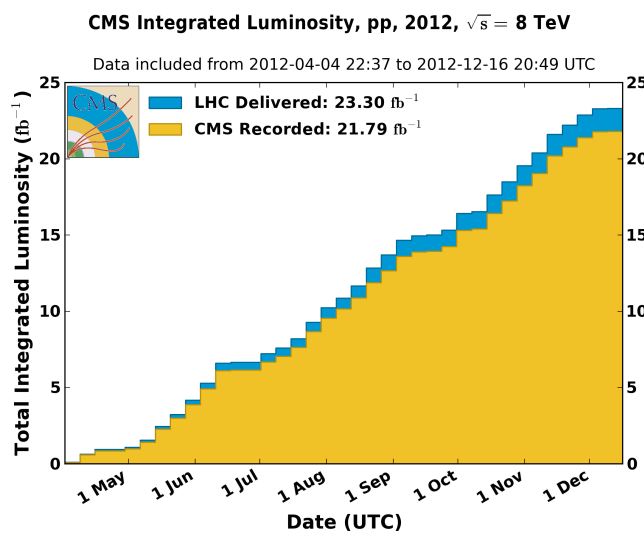


Figure 3.2.: The total integrated luminosity delivered to and collected by **CMS** during the 2012 8 TeV pp runs.

601 3.2. The CMS detector

602 The Compact Muon Solenoid (**CMS**) detector is one of two general purpose detectors
 603 at the **LHC** designed to search for new physics. The detector is designed to provide
 604 efficient identification and measurement of many physics objects including photons,
 605 electrons, muons, taus, and hadronic showers over wide ranges of transverse momentum
 606 and direction. Its nearly 4π coverage in solid angle allows for accurate measurement of
 607 global transverse momentum imbalance. These design factors give **CMS** the ability to
 608 search for direct production of **SUSY** particles at the TeV scale, making the search for
 609 Supersymmetric particles one of the highest priorities among the wide range of physics
 610 programmes at **CMS**.

611

612 **CMS** uses a right-handed Cartesian coordinate system with the origin at the interaction
 613 point and the z-axis pointing along the beam axis, the x-axis points radially inwards to
 614 the centre of the collider ring, with the y-axis points vertically upward. The azimuthal
 615 angle, ϕ ranging between $[-\pi, \pi]$ is defined in the x-y plane starting from the x-axis. The
 616 polar angle θ is measured from the z axis. The common convention in particle physics is
 617 to express an out going particle in terms of ϕ and its pseudorapidity defined as

$$\eta = -\log \tan \left(\frac{\theta}{2} \right). \quad (3.1)$$

618 The variable $\Delta R = \sqrt{\Delta\phi^2 + \Delta\eta^2}$ is commonly used to define angular distance
 619 between objects within the detector and additionally energy and momentum is typically
 620 measured in the transverse plane perpendicular to the beam line. These values are
 621 calculated from the x and y components of the object and are denoted as $E_T = E \sin \theta$
 622 and $p_T = \sqrt{p_x^2 + p_y^2}$.

623 3.2.1. Detector Subsystems

624 As the range of particles produced in pp collisions interact in different ways with mat-
 625 ter, **CMS** is divided into subdetector systems, which perform complementary roles to
 626 identify the identity, mass and momentum of the different physics objects present in
 627 each event. These detector sub-systems contained inside **CMS** are wrapped in layers

628 around a central 13 m long 4 T super conducting solenoid as shown in Figure 3.3. With
 629 the endcaps closed , CMS is a cylinder of length 22 m, diameter 15 m, and mass 12.5
 630 kilotons. A more detailed complete description of the detector can be found elsewhere [50].

631

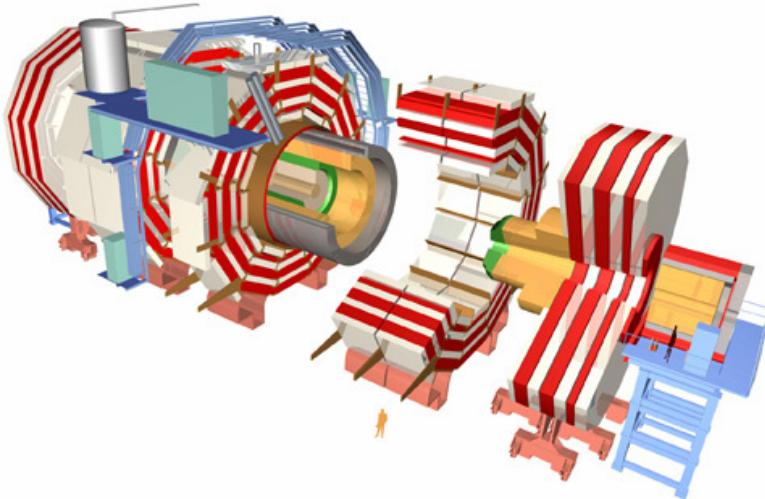


Figure 3.3.: A pictorial depiction of the CMS detector with the main detector subsystems labelled. [54]

632 3.2.2. Tracker

633 The inner-most subdetector of the barrel is the multi-layer silicon tracker, formed of a
 634 pixel detector component encased by layers of silicon strip detectors. The pixel detector
 635 consists of three layers of silicon pixel sensors providing measurements of the momentum,
 636 position coordinates of the charged particles as they pass, and the location of primary
 637 and secondary vertices between 4cm and 10cm transverse to the beam. Outside the pixel
 638 detector, ten cylindrical layers of silicon strip detectors extend the tracking system out to
 639 a radius of 1.20m from the beam line. The tracking system provides efficient and precise
 640 determination of the charges, momenta, and impact parameters of charged particles with
 641 the geometry of the tracker extending to cover a rapidity range up to $|\eta| < 2.5$.

642

643 The tracking system also plays a crucial part in the identification of jets originating
 644 from b-quarks through measurement of displaced secondary vertices, which is covered in
 645 more detail in Section (3.3.2). The identification of b-jets is important in many searches

646 for natural SUSY models and forms an important part of the inclusive search strategy
647 described within Section (4.2).

648 **3.2.3. Electromagnetic Calorimeter**

649 Immediately outside of the tracker, but still within the magnet core, sits the Electromag-
650 netic CALorimeter (**ECAL**). Covering a pseudorapidity up to $|\eta| < 3$ and comprising
651 of over 75,000 PbWO₄ (lead tungstate) crystals that scintillate as particles deposit energy,
652 the **ECAL** provides high resolution measurements of the electromagnetic showers from
653 photons, electrons in the detector.

654

655 Lead tungstate is used because of its short radiation length ($X_0 \sim 0.9\text{cm}$) and small
656 Molieré radius ($\sim 2.1\text{cm}$) leading to high granularity and resolution. It's fast scintillation
657 time ($\sim 25\text{ns}$) reduces the effects of pile-up due to energy from previous collisions still
658 being read out, and its radiation hardness gives it longevity. The crystals are arranged
659 in modules which surround the beam line in a non-projective geometry, angled at 3°
660 with respect to the interaction point to minimise the risk of particles escaping down the
661 cracks between the crystals.

662

663 The **ECAL** is primarily composed of two sections, the Electromagnetic CALorime-
664 ter Barrel (**EB**) which extends in pseudo-rapidity to $|\eta| < 1.479$ with a crystal front
665 cross section of $22 \times 22\text{ mm}^2$ and a length of 230 mm corresponding to 25.8 radia-
666 tion lengths, and the Electromagnetic CALorimeter Endcap (**EE**) covering a rapidity
667 range of $1.479 < |\eta| < 3.0$, which consists of two identical detectors on either side of
668 the **EB**. A lead-silicon sampling ‘pre-shower’ detector Electromagnetic CALorimeter
669 pre-Shower (**ES**) is placed before the endcaps to aid in the identification of neutral pions.
670 Their arrangement are shown in Figure 3.4.

671

672 Scintillation photons from the lead tungstate crystals are instrumented with Avalanche
673 Photo-Diodes (**APD**) and Vacuum Photo-Triodes (**VPT**) located in the **EB** and **EE**
674 respectively, converting the scintillating light into an electric signal which is consequently
675 used to determine the amount of energy deposited within the crystal . These instruments
676 are chosen for their resistance under operation to the strong magnetic field of **CMS**. The
677 scintillation of the **ECAL** crystals as well as the response of the **APDs** varies as a function

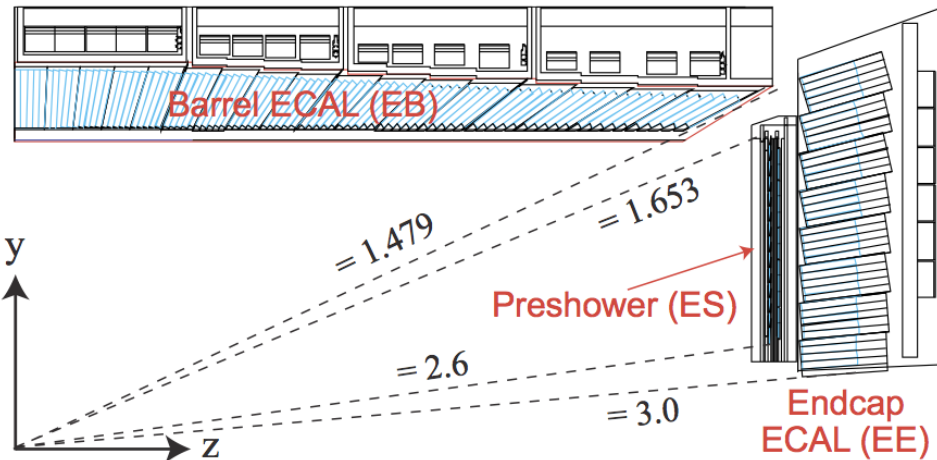


Figure 3.4.: Illustration of the CMS ECAL showing the arrangement of the lead tungstate crystals in the EB and EE. The ES is also shown and is located in front of the EE [55].

678 of temperature and so cooling systems continually maintain an overall constant ECAL
679 temperature $\pm 0.05^\circ C$.

680 3.2.4. Hadronic Calorimeter

681 Beyond the ECAL lies the Hadronic CALorimeter (HCAL) which is responsible for
682 the accurate measurement of hadronic showers, crucial for analyses involving jets or
683 missing energy signatures. The HCAL is a sampling calorimeter which consists of al-
684 ternating layers of brass absorber and plastic scintillator, except in the hadron forward
685 ($3.0 < |\eta| < 5.0$) region in which steel absorbers and quartz fibre scintillators are used
686 because of their increased radiation tolerance. Hadron showers are initiated in the
687 absorber layers inducing scintillation in the plastic scintillator tiles. These scintillation
688 photons are converted by wavelength shifting fibres for read-out by hybrid photodiodes.
689

690 The HCAL's size is constrained to a compact size by the presence of the solenoid,
691 requiring the placement of an additional outer calorimeter on the outside of the solenoid
692 to increase the sampling depth of the HCAL. A schematic of the HCAL can be seen in
693 Figure 3.5.

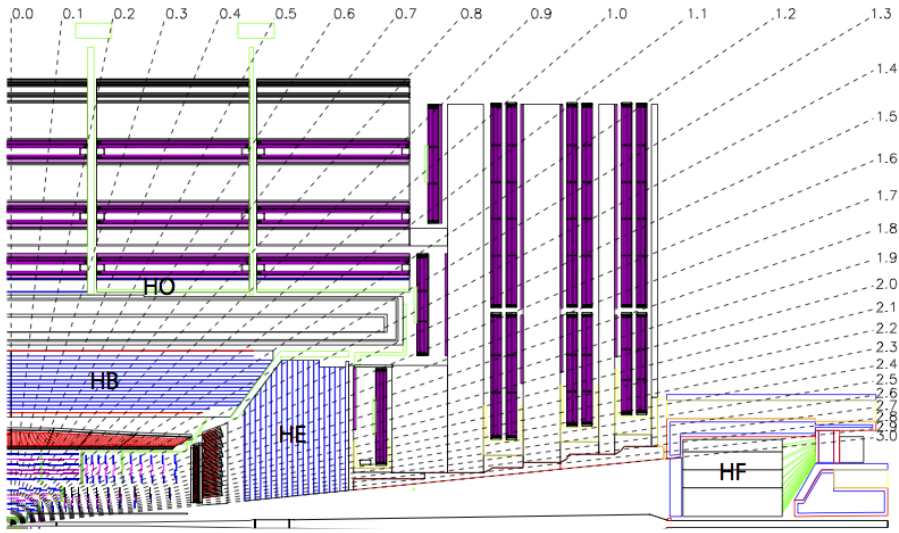


Figure 3.5.: Schematic of the hadron calorimeters in the r - z plane, showing the locations of the **HCAL** components and the **HF**. [50].

695 The **HCAL** covers the range $|\eta| < 5$ and consists of four subdetectors: the Hadron
 696 Barrel (**HB**) $|\eta| < 1.3$, the Hadron Outer (**HO**), the Hadron Endcaps (**HE**) $1.3 < |\eta| < 3.0$
 697 and the Hadron Forward (**HF**). The **HB** is contained between the outer edge of the **ECAL**
 698 and the inner edge of the solenoid, formed of 36 azimuthal wedges it is split between
 699 two half-barrel segments. Each wedge is segmented into four azimuthal angle (ϕ) sectors,
 700 and each half-barrel is further segmented into 16 η towers. The electronic readout chain,
 701 channels the light from the active scintillator layers from one ϕ -segment and all η -towers
 702 of a half-barrel to a Hybrid Photo Diode (**HPD**).

703 The relatively short number of interaction lengths (λ_l , the distance a hadron will
 704 travel through the absorber material before it has lost $\frac{1}{e}$ of its energy) within the **HB**,
 705 the lowest being $\lambda_l = 5.82$ for $|\eta| = 0$, facilitates the need for the ‘tail catching’ **HO**
 706 to increase the sampling depth in the central barrel rapidity region $|\eta| < 1.3$ to 11
 707 interaction lengths . Significant fractions of the hadrons energy will be deposited in the
 708 **ECAL** as it passed through the detector. Therefore measurements of hadron energies
 709 in the central regions $|\eta| < 3.0$ use both the **ECAL** and **HCAL** to reconstruct the true
 710 energy from showering hadrons.

711 **3.2.5. Muon Systems**

712 Muons being too massive to radiate away energy via Bremsstrahlung, interact little in
713 the calorimeters and mostly pass through the detector until they reach the system of
714 muon detectors which forms the outer most part of the **CMS** detector.

715 Outside of the superconducting solenoid are four muon detection layers interleaved
716 with the iron return yokes which measure the muons energy via ionisation of gas within
717 detector elements. Three types of gaseous chamber are used. The Drift Tube (**DT**),
718 Cathode Stripe Chamber (**CSC**), and Resistive Plate Chamber (**RPC**) systems provide
719 efficient detection of muons with pseudo-rapidity $|\eta| < 2.4$. The best reconstruction
720 performance is obtained when the muon chamber is combined with the inner tracking
721 information to determine muon trajectories and their momenta [56].

722

723 **3.3. Event Reconstruction and Object Definition**

724 The goal of event reconstruction is to take the raw information recorded by the detector
725 and to compute from it higher-level quantities which can be used at an analysis level.
726 These typically correspond to an individual particle’s energy and momenta, or groups of
727 particles which shower in a narrow cone and the overall global energy and momentum
728 balance of the event. The reconstruction of these objects are described in great detail in
729 [57], however covered below are brief descriptions of those which are most relevant to the
730 analysis detailed in Chapter 4.

731 **3.3.1. Jets**

732 Quarks and gluons are produced copiously at the LHC in the hard scattering of partons.
733 As these quarks and gluons fragment, they hadronise and decay into a group of strongly
734 interactive particles and their decay products. These streams of particles travel in the
735 same direction, as they have been “boosted” by the momentum of the primary hadron.
736 These collections of decay products are reconstructed and identified together as a “jet”.

737 At **CMS** jets are reconstructed from energy deposits in the detector using the anti-kt
738 algorithm [58] with size parameter $\Delta R = 0.5$. The anti-kt jet algorithm clusters jets by
739 defining a distance between hard (high p_T) and soft (low p_T) particles such that soft

740 particles are preferentially clustered with hard particles before being clustered between
741 themselves. This produces jets which are robust to soft particle radiation from the pile-up
742 conditions experienced at the **LHC**.

743

744 There are two main type of jet reconstruction used at **CMS**, Calorimeter (Calo) and
745 Particle Flow (PF) jets [59]. Calorimeter jets are reconstructed using both the **ECAL**
746 and **HCAL** cells, combined into calorimeter towers . These calorimeter towers consist of
747 geometrically matched **HCAL** cells and **ECAL** crystals. Electronics noise is suppressed by
748 applying a threshold to the calorimeter cells, with pile-up effects reduced by a requirement
749 placed on the tower energy [60]. Calorimter jets are the jets used within the analyses
750 described in this thesis.

751 PF jets are formed from combining information from all of the **CMS** subdetectors
752 systems to determine which final state particles are present in the event. Generally,
753 any particle is expected to produce some combination of a track in the silicon tracker,
754 a deposit in the calorimeters, or a track in the muon system. The PF jet momentum
755 and spatial resolutions are greatly improved with respect to calorimeter jets, as the use
756 of the tracking detectors and of the high granularity of **ECAL** allows resolution and
757 measurement of charged hadrons and photons inside a jet, which together constitute \sim
758 85% of the jet energy [61].

759 The jets reconstructed by the clustering algorithm in **CMS** typically have an energy
760 that differs to the ‘true’ energy measured by a perfect detector. This stems from the
761 non-linear and nonuniform response of the calorimeters as well as other residual effects
762 including pile-up and underlying events, and therefore additional corrections are applied
763 to recover a uniform relative response as a function of pseudo-rapidity. These are applied
764 as separate sub corrections [62].

- 765 • A PU correction is first applied to the jet. It subtracts the average extra energy
766 deposited in the jet that comes from other vertices present in the event and is
767 therefore not part of the hard jet itself.
- 768 • p_T and η dependant corrections derived from Monte Carlo simulations are used to
769 account for the non-uniform response of the detector.
- 770 • p_T and η residual corrections are applied to data only to correct for difference
771 between data and Monte Carlo. The residual is derived from QCD dijet samples
772 and the p_T residual from $\gamma+$ jet and $Z+$ jets samples in data.

⁷⁷³ **3.3.2. B-tagging**

⁷⁷⁴ The decays of b quarks are suppressed by small CKM matrix elements. As a result, the
⁷⁷⁵ lifetimes of b-flavoured hadrons, produced in the fragmentation of b quarks, are relatively
⁷⁷⁶ long; \mathcal{O} 1ps. The identification of jets origination from b quarks is very important for
⁷⁷⁷ searches for new physics and for measurements of standard model processes.

⁷⁷⁸

⁷⁷⁹ Many different algorithms developed by CMS select b-quark jets based on variables
⁷⁸⁰ such as the impact parameters of the charged-particle tracks, the properties of recon-
⁷⁸¹ structed decay vertices, and the presence or absence of a lepton, or combinations thereof
⁷⁸² [63]. One of the most efficient of which is the Combined Secondary Vertex (CSV) which
⁷⁸³ operates based on secondary vertex and track-based lifetime information, benchmarked
⁷⁸⁴ in ‘Loose’, ‘Medium’ and ‘Tight’ working points, of which the medium point is the tagger
⁷⁸⁵ used within the α_T search detailed in Section (4.1).

⁷⁸⁶ Using the CSV tagger, a likelihood-based discriminator distinguishes between jets
⁷⁸⁷ from b-quarks, and those from charm or light quarks and gluons, which is shown in Figure
⁷⁸⁸ 3.6. The minimum thresholds on the discriminator for each working point correspond to
⁷⁸⁹ the misidentification probability for light-parton jets of 10%, 1%, and 0.1%, respectively,
⁷⁹⁰ in jets with an average p_T of about 80 GeV.

⁷⁹¹ The b-tagging performance is evaluated to measure the b-jet tagging efficiency ϵ_b ,
⁷⁹² and the misidentification probability of charm ϵ_c and light-parton jets ϵ_s . The tagging
⁷⁹³ efficiencies for each of these three jet flavours are compared between data and MC
⁷⁹⁴ simulation, from which a series of p_T and $|\eta|$ binned jet corrections are determined,

$$SF_{b,c,s} = \frac{\epsilon_{b,c,s}^{data}}{\epsilon_{b,c,s}^{MC}}. \quad (3.2)$$

⁷⁹⁵ These are collectively named ‘Btag Scale Factors’ and allow MC simulation to accu-
⁷⁹⁶ rately reflect the running conditions and performance of the tagging algorithm in data.
⁷⁹⁷ Understanding of the b-tagging efficiency is essential in order to minimise systematic
⁷⁹⁸ uncertainties in physics analyses that employ b-tagging.

⁷⁹⁹

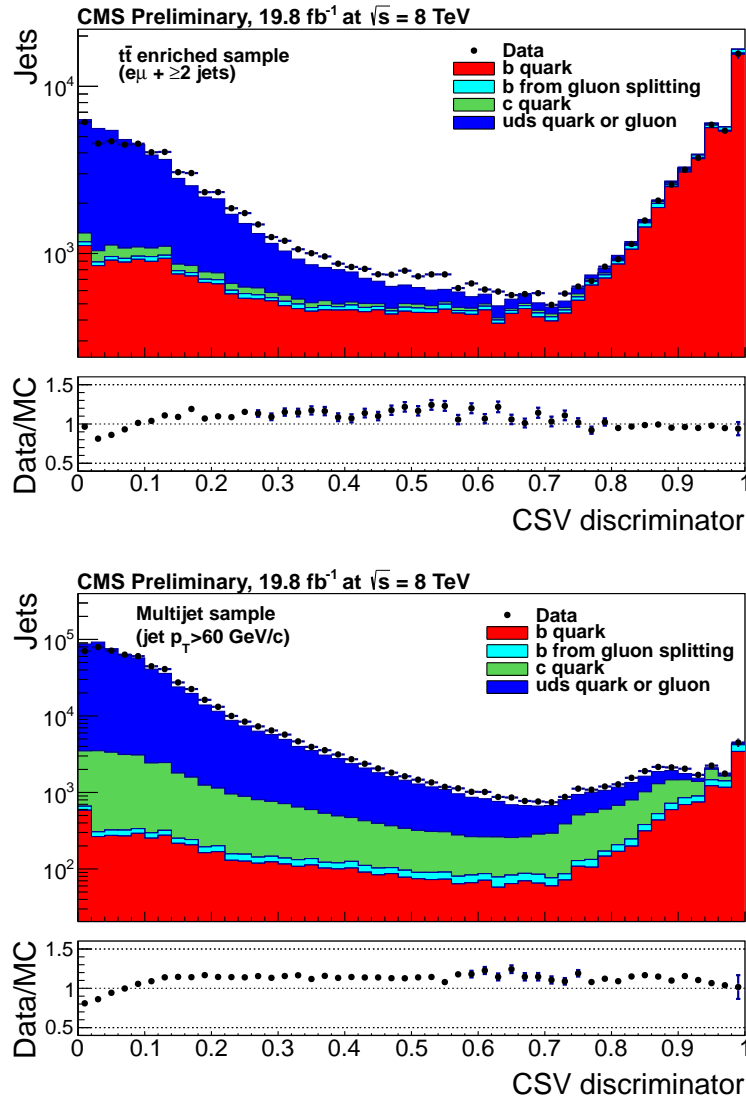


Figure 3.6.: CSV algorithm discriminator values in enriched $t\bar{t}$ (top) and inclusive multi-jet samples (bottom) for b,c and light flavoured jets [64]. Working points are determined from the misidentification probability for light-parton jets to be tagged as a b-jet and are given as 0.244, 0.679 and 0.898 for L,M and T working points respectively.

800 The b-tagging efficiency is measured in data using several methods applied to multi
 801 jet events, primarily based on a sample of jets enriched in heavy flavour content. One
 802 method requires the collection of events with a soft muon within a cone $\Delta R < 0.4$ around
 803 the jet axis. Because the semileptonic branching fraction of b hadrons is significantly
 804 larger than that for other hadrons, these jets are more likely to arise from b quarks than
 805 from another flavour, with the resultant momentum component of the muon transverse
 806 to the jet axis larger for muons from b-hadron decays than from light or charm jets.

807 Additionally the performance of the tagger can also be benchmarked in $t\bar{t}$ events where
 808 in the SM, the top quark is expected to decay to a W boson and a b quark about 99.8%
 809 of the time [1]. Further selection criteria is applied to these events to further enrich the
 810 b quark content of these events. The methods to identify b-jets in data are discussed
 811 in great detail at [65]. The jet flavours are determined in simulation using truth level
 812 information and are compared to data to determine the correction scale factors (SF_b),
 813 which are displayed for the CSVM tagger in Figure 3.7.

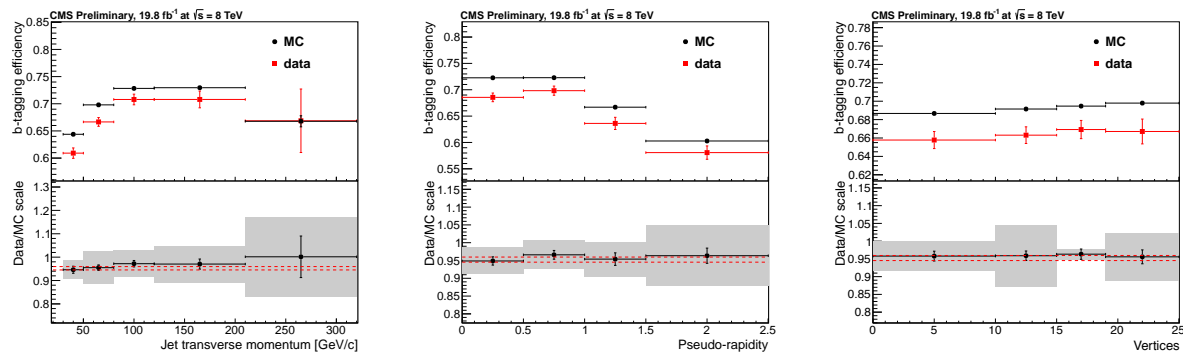


Figure 3.7.: Measured in $t\bar{t} \rightarrow$ di-lepton events using the CSVM tagger: (upper panels) b-tagging efficiencies and (lower panels) data/MC scale factor SF_b as a function of (left) jet p_T , (middle) jet $|\eta|$ and (right) number of primary vertices. In the lower panels, the grey filled areas represent the total statistical and systematic uncertainties, whereas the dotted lines are the average SF_b values within statistical uncertainties.

814 The measurement of the misidentification probability for light-parton jets relies on
 815 the inversion of tagging algorithms, selecting non-b jets using the same variables and
 816 techniques used in benchmarking the b-tagging efficiency. The scale factors (SF_s) to be
 817 applied to MC are shown in Figure 3.8 for the CSVM tagger.

818 3.4. Triggering System

819 With bunch crossings separated by just 25 ns, the rate at which data from all collisions
 820 would have to be written out and processed would be unfeasible. A two-tiered triggering
 821 system is applied at CMS in order to cope with the high collision rate of protons. The
 822 CMS trigger is designed to use limited information from each event to determine whether
 823 to record the event, reducing the rate of data taking to manageable levels whilst ensuring
 824 a high efficiency of interesting physics object events are selected.

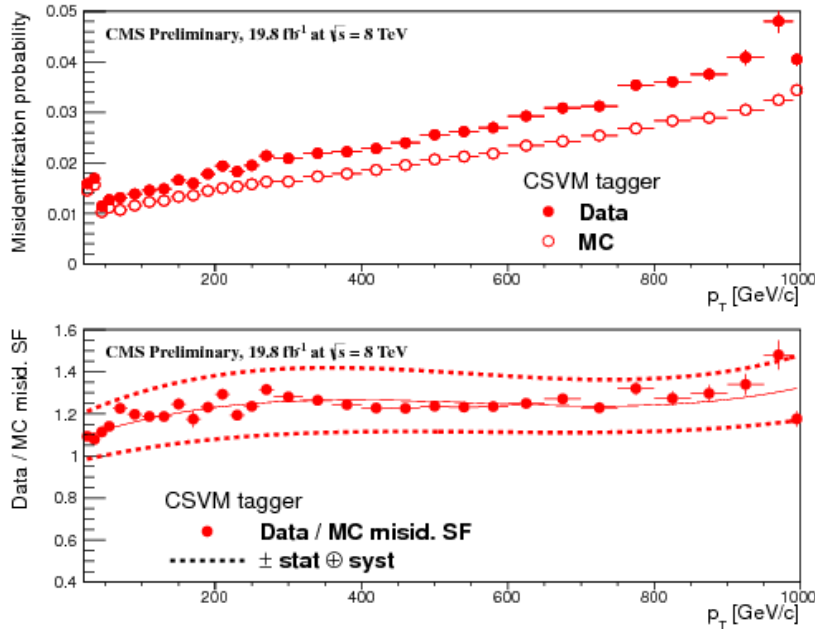


Figure 3.8.: For the **CSVM** tagging criterion: (top) misidentification probability in data (filled circles) and simulation (open circles); (bottom) scale factor for the misidentification probability. The last p_T bin in each plot includes all jets with $p_T > 1000$ GeV. The solid curve is the result of a polynomial fit to the data points. The dashed curves represent the overall statistical and systematic uncertainties on the measurements.

825 The **L1** is a pipelined, dead-timeless system based on custom-built electronics [66],
 826 and is a combination of several sub systems which is shown pictorially in Figure 3.9. The
 827 **L1** system is covered in more detail within the following section along with a description
 828 of the service work undertaken by the author to benchmark the performance of the **L1**
 829 calorimeter trigger during the 2012 8 TeV run period.

830 The Higher Level Trigger (**HLT**) is a large farm of commercial computers [67]. The
 831 **HLT** processes events with software reconstruction algorithms that are more detailed,
 832 giving performance more similar to the reconstruction used offline. The **HLT** reduces
 833 the event rate written to disk by a factor of ~ 500 (~ 200 Hz). The recorded events are
 834 transferred from **CMS** to the **CERN** computing centre, where event reconstruction is
 835 performed, and then distributed to **CMS** computing sites around the globe for storage
 836 and analysis.

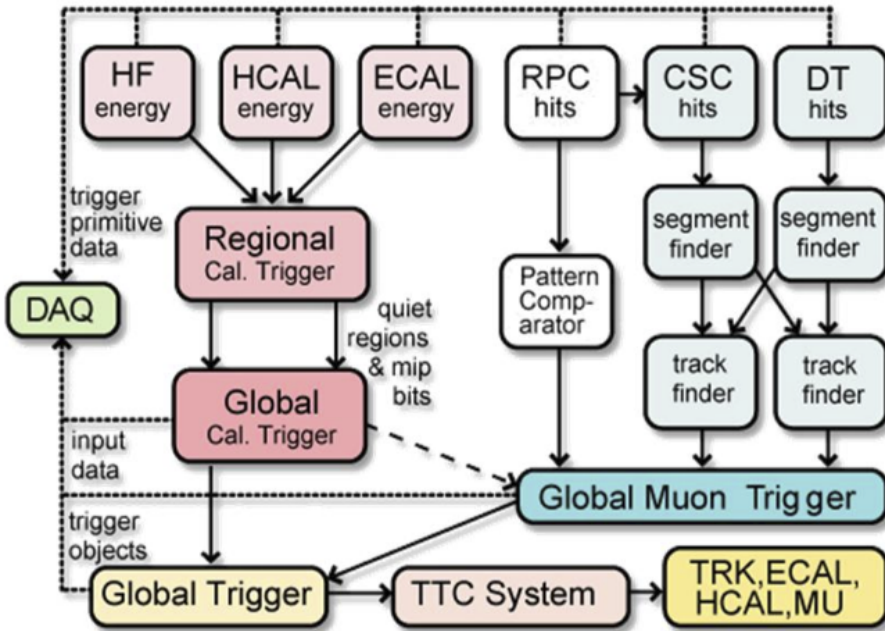


Figure 3.9.: The CMS L1 Trigger system.

3.4.1. The Level-1 Trigger

The L1 trigger reduces the rate of events collected from 40 MHz to ~ 100 kHz using information from the calorimeters and muon chambers, but not the tracker. A tree system of triggers is used to decide whether to pass on an event to the HLT for further reconstruction. Firstly the calorimeter and muon event information is kept separate, with local reconstruction of objects ($\mu, e, \gamma, \text{jets}$) performed by the Regional Calorimeter Trigger (RCT) and Regional Muon Trigger (RMT) respectively. The RCT generates up to 72 isolated and non-isolated electromagnetic objects. These are sorted by rank, which is equivalent to transverse energy E_T , with the four highest ranked electromagnetic objects being passed via the Global Calorimeter Trigger (GCT) and Global MuonTrigger (GMT) to the Global Trigger (GT).

In the L1 GCT, coarse measurements of the energy deposited in the electromagnetic and hadronic calorimeters are combined and by using sophisticated algorithms the following physics objects are formed:

- isolated and non-isolated electromagnetic objects (e and γ);
- hadronic jets in the central and forward sections of the hadronic calorimeters;

- 853 • hadronically decaying tau leptons;
- 854 • total transverse energy (E_T), the scalar sum of the energy measured at L1, and
855 missing transverse energy (\cancel{E}_T), defined as the vector sum of the energy of L1
856 objects;
- 857 • total transverse jet energy (H_T), the scalar sum of the energy of all L1 jet objects,
858 and missing transverse jet energy (\cancel{H}_T), defined as the vector sum of the energy of
859 L1 jets, are calculated from uncorrected L1 jets.

860 In addition quantities suitable for triggering minimum bias events, forward physics and
861 beam background events are calculated. Additionally relevant muon isolation information
862 is also passed on to the **GMT** for decisions involving the muon triggers where it is
863 combined with information from across the three muon sub-systems. The resultant final
864 accept/reject decision at **L1** is then performed by the **GT** based on the objects received
865 from the **GCT** and **GMT** (e/γ , μ , jets, E_T , \cancel{E}_T , H_T).

866 The L1 trigger is therefore of upmost importance to the functioning of the detector.
867 Without a high-performing trigger and a good understanding of it's performance, there
868 would be no data to analyse. Observations of how the L1 trigger performance is affected
869 by changing **LHC** running conditions over the 2012 run period and also the introduction
870 of a jet seed threshold to the L1 jet trigger algorithm is presented in the following Sections
871 (3.4.2 - 3.4.6).

872 3.4.2. L1 Trigger Jet Algorithm

873 The L1 jet trigger uses the transverse energy sums computed in the calorimeter (both
874 hadronic and electromagnetic) trigger regions. Each region consists of 4×4 trigger tower
875 windows, spanning a region of $\Delta\eta \times \Delta\phi = 0.087 \times 0.087$ in pseudorapidity-azimuth. The
876 jet trigger uses a 3×3 calorimeter region (112 trigger towers) sliding window technique
877 which spans the full (η, ϕ) coverage of the **CMS** calorimeter as shown in Figure 3.10.

878 In forming a L1 jet is it required that the central region to be higher than the eight
879 neighbouring regions $E_{T\text{central}} > E_{T\text{surround}}$. Additionally a minimum threshold of 5 GeV
880 on $E_{T\text{central}}$ was introduced during the 2012 run period to suppress noise from pile-up,
881 the effects of which are shown in Section (3.4.4).

882 The L1 jets are characterised by the E_T , summed over the 3×3 calorimeter regions,
883 which corresponds to 12×12 trigger towers in barrel and endcap or 3×3 larger **HF**

884 towers in the **HF**. The ϕ size of the jet window is the same everywhere, whilst the η
885 binning gets somewhat larger at high η due to calorimeter and trigger tower segmentation.
886 The jets are labelled by (η, ϕ) indexes of the central calorimeter region.

887 Jets with $|\eta| > 3.0$ are classified as forward jets, whereas those with $|\eta| < 3.0$ are
888 classified as central. The four highest energy central, forward and τ jets in the calorimeter
889 are passed through Look Up Table (**LUT**)'s, which apply a programmable η -dependent
890 jet energy scale correction. These are then used to make L1 trigger decisions.

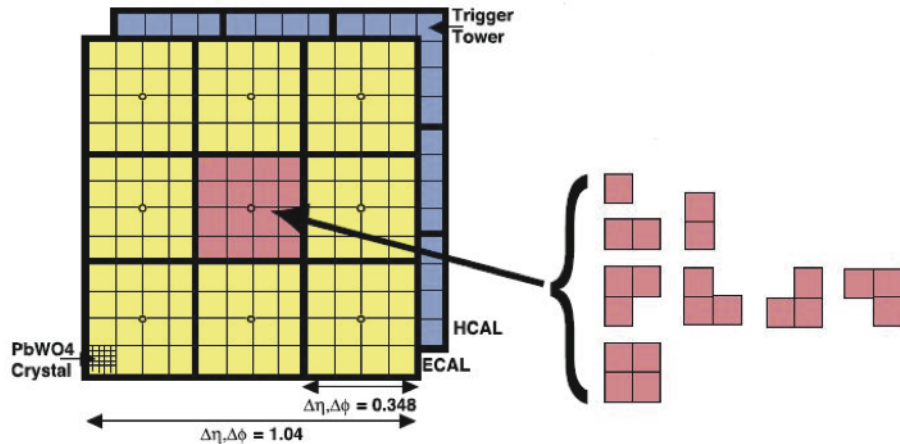


Figure 3.10.: Illustration of the Level-1 jet finding algorithm.

891 The performance of the L1 jets is evaluated with respect to offline jets, which are
892 taken from the standard Calo jet and the PF jet reconstruction algorithms of **CMS**.
893 Jets are corrected for pile-up and detector effects as described in [3.3.1](#). A moderate
894 level of noise rejection is applied to the offline jets by selecting jets passing the “loose”
895 identification criteria for both Calo and PF. These criteria are summarised in Appendix
896 ([A.1](#)).

897 3.4.3. Measuring L1 Jet Trigger Efficiencies

898 The L1 jet efficiency is defined as the fraction of leading offline jets which were matched
899 with a L1 tau or central jet above a certain trigger threshold, divided by all the leading
900 offline jets in the event. This quantity is then plotted as a function of the offline jet E_T ,
901 η and ϕ .

902 The efficiency is determined by matching the L1 and reconstructed offline jets spatially
903 in $\eta - \phi$ space. This is done by calculating the minimum separation in ΔR between the

highest offline reconstructed jet in E_T ($E_T > 10$ GeV, $|\eta| < 3$) and any L1 jet. A jet will be matched if this value is found to be < 0.5 . Should more than one jet satisfy this, the jet closest in ΔR is taken as the matched jet. The matching efficiency is close to 100%, above ? 30(45) GeV for run 2012B(C) data (see Appendix (??)).

Each efficiency curve is fitted with a function which is the cumulative distribution function of an Exponentially Modified Gaussian (EMG) distribution:

$$f(x; \mu, \sigma, \lambda) = \frac{\lambda}{2} \cdot e^{\frac{\lambda}{2}(2\mu + \lambda\sigma^2 - 2x)} \cdot \text{erfc}\left(\frac{\mu + \lambda\sigma^2 - x}{\sqrt{2}\sigma}\right) \quad (3.3)$$

where erfc is the complementary error function defined as:

$$\text{erfc}(x) = 1 - \text{erf}(x) = \frac{2}{\sqrt{\pi}} \int_x^\infty e^{-t^2} dt.$$

In this functional form, the parameter μ determines the point of 50% of the plateau efficiency and the σ gives the resolution. This parametrisation is used to benchmark the efficiency at the plateau, the turn-on points and resolution for each L1 Jet trigger. The choice of function is purely empirical. Previous studies used the error function alone, which described the data well at high threshold values but could not describe the efficiencies well at lower thresholds [68].

The efficiency turn-on curves for various L1 jet thresholds are evaluated as a function of the offline reconstructed jet E_T for central jets with $|\eta| < 3$. These are measured using single isolated μ triggers which have high statistics, and are orthogonal and therefore unbiased to the hadronic triggers under study. The efficiency is calculated with respect to offline Calo and PF Jets in Figure 3.11. Table 3.1 shows the values of these parameters, calculated for three example L1 single jet triggers taken from 2012 8 TeV data.

The results from the L1 single jet triggers shows good performance for both Calo and PF jets. A better resolution for Calo jets with respect to L1 jets quantities is observed. This effect is due to Calo jet reconstruction using the same detector systems as in L1 jets, whereas with PF jet construction using tracker and muon information, a more smeared resolution when compared to L1 is expected.

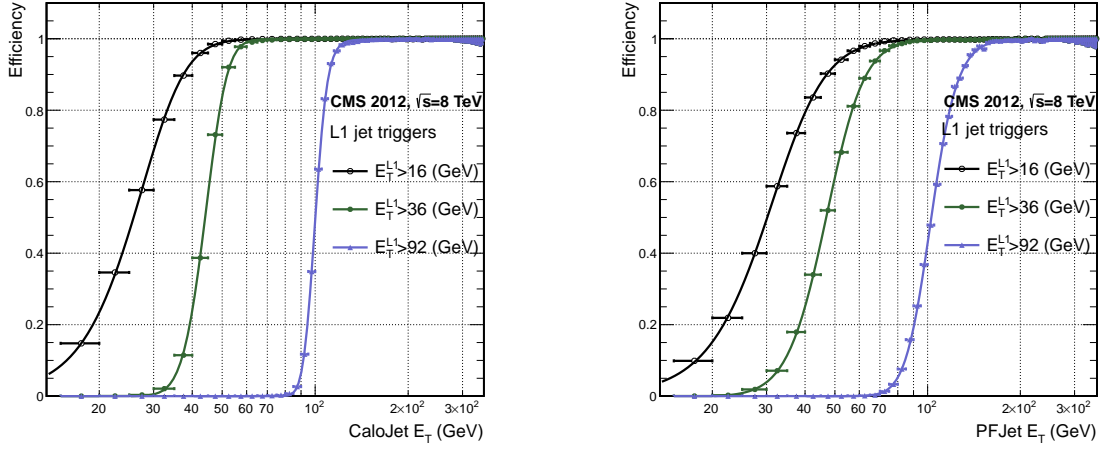


Figure 3.11.: L1 jet efficiency turn-on curves as a function of the offline CaloJet E_T (left) and PFJet E_T (right), measured in 2012 Run Period C data and collected with an isolated single μ data sample.

Trigger	Calo		PF	
	μ	σ	μ	σ
L1_SingleJet16	21.09 ± 0.03	7.01 ± 0.02	22.17 ± 0.04	7.83 ± 0.03
L1_SingleJet36	41.15 ± 0.05	5.11 ± 0.02	39.16 ± 0.06	8.04 ± 0.03
L1_SingleJet92	95.36 ± 0.13	5.62 ± 0.03	90.85 ± 0.19	11.30 ± 0.10

Table 3.1.: Results of a cumulative EMG function fit to the turn-on curves for L1 single jet triggers in run 2012 Run Period C, measured in an isolated μ data sample. The turn-on point, μ , and resolution, σ , of the L1 jet triggers are measured with respect to offline Calo Jets (left) and PF Jets (right).

3.4.4. Effects of the L1 Jet Seed

Between run period B and C of the 2012 data taking period, a jet seed threshold was introduced into the L1 trigger jet algorithm. There was previously no direct requirement made on the energy deposited in the central region. The introduction of a jet seed threshold required that the central region have $E_T \geq 5$ GeV, and was introduced to counteract the effects of high pile up running conditions which create a large number of soft non-collimated jets, that are then added to the jets from the primary interaction or other soft jets from other secondary interactions [69]. This in turn causes a large increase in trigger rate due to the increase in the likelihood that the event causes the L1 trigger to fire. This was implemented to maintain trigger thresholds by cutting the rate of events recorded without significant reduction in the efficiency of physics events of interest.

The effect of the introduction of this jet seed threshold between these two run periods is benchmarked through a comparison of the efficiency of the L1 jet triggers with respect to offline Calo jets shown in Figure 3.12, and the L1 H_T trigger efficiency in Figure 3.14 which is compared to offline H_T constructed from Calo jets with $E_T \geq 40\text{GeV}$.

To negate any effects from different pile-up conditions in the run periods, the efficiencies are measured in events which contain between 15 and 20 primary vertices as defined in Appendix (A.2).

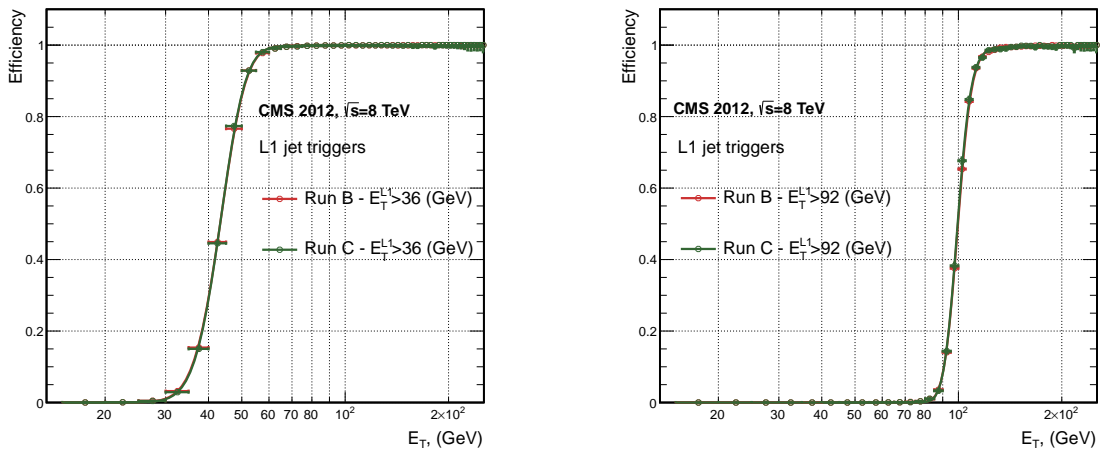


Figure 3.12.: L1 jet efficiency turn-on curves as a function of the offline CaloJet E_T , measured for the L1 SingleJet 36 and 92 trigger in 2012 run period B and C collected with an isolated single μ' sample.

It can be seen that the performance of the $E_T > 36, 92$ single jet are almost identical, with the jet seed having no measurable effect on these triggers as shown in Table 3.2 .

Trigger	2012B		2012C	
	μ	σ	μ	σ
L1_SingleJet36	40.29 ± 0.04	5.34 ± 0.02	40.29 ± 0.11	5.21 ± 0.05
L1_SingleJet92	94.99 ± 0.09	5.93 ± 0.06	94.82 ± 0.29	5.74 ± 0.18

Table 3.2.: Results of a cumulative EMG function fit to the turn-on curves for L1 single jet triggers in the 2012 run period B and C, preselected on an isolated muon trigger. The turn-on point μ and resolution σ of the L1 jet triggers are measured with respect to offline Calo Jets in run B (left) and run C (right).

For the H_T triggers, a large increase in rate during high pile-up conditions is expected. This is due to the low energy threshold required for a jet to be added to the L1 H_T sum,

which is compiled from all uncorrected L1 jets formed in the RCT. The introduction of the jet seed threshold removes the creation of many of these soft low E_T jets, thus lowering the H_T calculation at L1. The effect on the trigger cross section for L1 H_T 150 trigger can be seen in Figure 3.13.

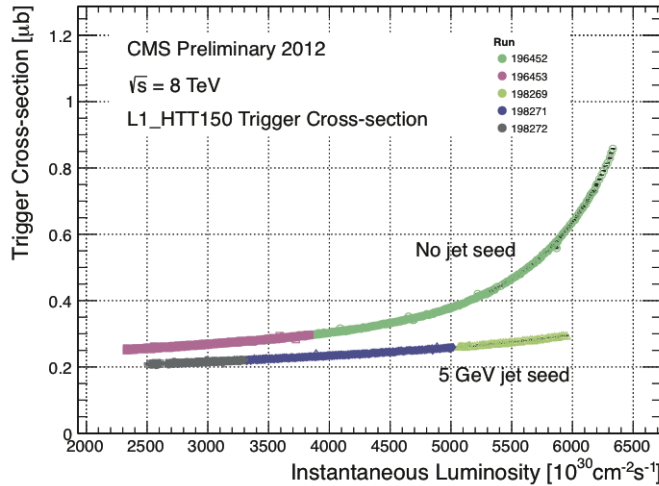


Figure 3.13.: Trigger cross section for the L1HTT150 trigger path. Showing that a 5 GeV jet seed threshold dramatically reduces the dependance of cross section on the instantaneous luminosity for L1 H_T triggers [70].

Different behaviours for the trigger turn ons between these run periods are therefore expected. The turn on point is observed to shift to higher H_T values after the introduction of the jet seed threshold, whilst having a sharper resolution due to less pile-up jets being included the H_T sum, the results are shown in Table 3.3.

Trigger	2012B		2012C	
	μ	σ	μ	σ
L1 HT-100	157.5 ± 0.08	32.9 ± 0.08	169.8 ± 0.08	28.7 ± 0.03
L1 H1-150	230.9 ± 0.02	37.3 ± 0.01	246.4 ± 0.16	31.8 ± 0.05

Table 3.3.: Results of a cumulative EMG function fit to the turn-on curves for H_T in run 2012 B and C, preselected on an isolated single μ trigger. The turn-on point μ , resolution σ of the L1 H_T triggers are measured with respect to offline H_T formed from CaloJets with a $E_T \geq 40$ in run period B (left) and C (right).

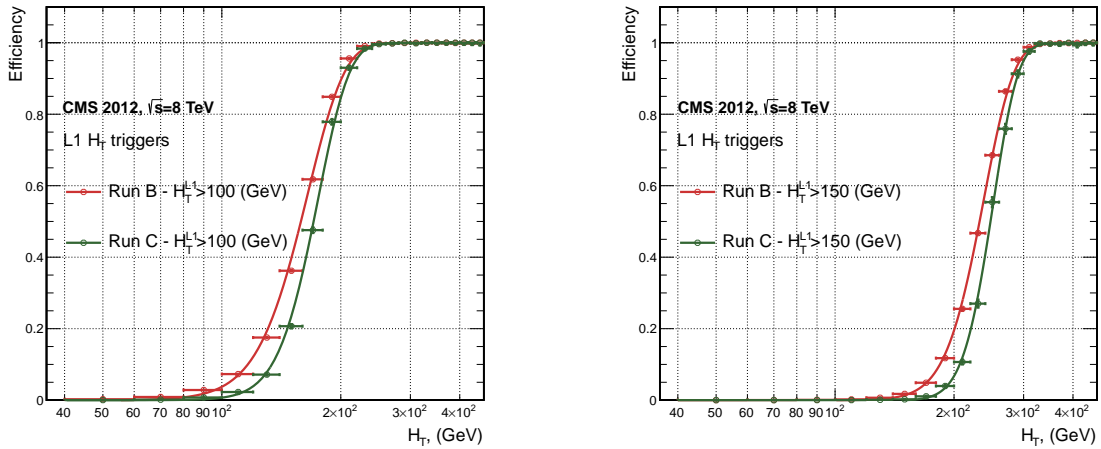


Figure 3.14.: L1 H_T efficiency turn-on curves as a function of the offline CaloJet H_T , measured for the L1 H_T 100 and 150 trigger during the run 2012 B and C collected using an isolated single μ triggered sample.

958 3.4.5. Robustness of L1 Jet Performance against Pile-up

959 The performance of the L1 single jet triggers is evaluated in different pile-up conditions
960 to benchmark any dependence on pile-up. Three different pile-up bins of 0-10, 10-20 and
961 >20 vertices are defined, reflecting the low, medium and high pile-up running conditions
962 at CMS in 2012. This is benchmarked relative to Calo and PF jets for the run 2012 C
963 period where the jet seed threshold is applied, with L1 single jet thresholds of 16, 36 and
964 92 GeV, shown in Figure 3.15. The results of fits to these efficiency turn-on curves are
965 given in Table 3.4 and Table 3.5 for Calo and PF jets respectively.

Vertices	0-10		11-20		> 20	
	μ	σ	μ	σ	μ	σ
L1_SingleJet16	19.9 ± 0.1	6.1 ± 0.3	20.8 ± 0.1	6.5 ± 0.1	22.3 ± 0.2	7.5 ± 0.1
L1_SingleJet36	41.8 ± 0.1	4.6 ± 0.1	40.9 ± 0.1	5.1 ± 0.1	40.6 ± 0.6	5.9 ± 0.2
L1_SingleJet92	95.9 ± 0.2	5.4 ± 0.1	95.2 ± 0.2	5.6 ± 0.1	94.5 ± 0.6	6.2 ± 0.3

Table 3.4.: Results of a cumulative EMG function fit to the efficiency turn-on curves for L1 single jet triggers in the 2012 run period C, measured from isolated μ triggered data. The turn-on point, μ , and resolution, σ , of the L1 jet triggers are measured with respect to offline Calo jets in low (left), medium (middle) and high (right) pile-up conditions.

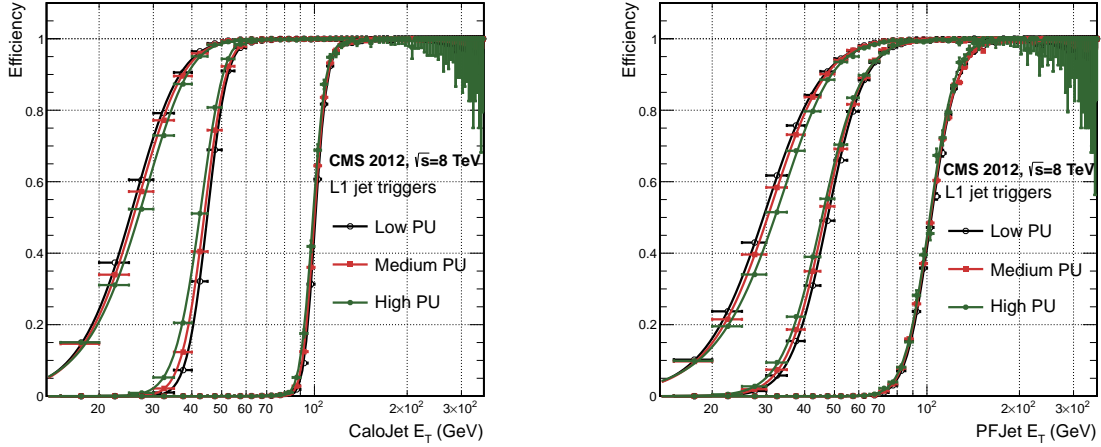


Figure 3.15.: L1 jet efficiency turn-on curves as a function of the leading offline E_T Calo (left) and PF (right) jet, for low, medium and high pile-up conditions.

Vertices	0-10		11-20		> 20	
	μ	σ	μ	σ	μ	σ
L1_SingleJet16	21.1 ± 0.1	7.16 ± 0.05	22.34 ± 0.1	7.9 ± 0.1	24.6 ± 0.2	9.5 ± 0.1
L1_SingleJet36	39.6 ± 0.1	7.4 ± 0.1	38.4 ± 0.1	7.4 ± 0.1	37.1 ± 0.2	7.5 ± 0.1
L1_SingleJet92	91.6 ± 0.3	11.3 ± 0.2	90.4 ± 0.3	11.2 ± 0.1	92.0 ± 0.9	12.1 ± 0.4

Table 3.5.: Results of a cumulative EMG function fit to the efficiency turn-on curves for Level-1 single jet triggers in the 2012 run period C, measured from isolated μ triggered data. The turn-on point, μ , and resolution, σ , of the L1 jet triggers are measured with respect to offline PF jets in low (left), medium (middle) and high (right) pile-up conditions.

966 No significant drop in efficiency is observed in the presence of a high number of
 967 primary vertices. The increase in hadronic activity in higher pile-up conditions, combined
 968 with the absence of pile-up subtraction for L1 jets, results in the expected observation of
 969 a decrease in the μ value of the efficiency turn-ons as a function of pile-up, while the
 970 resolution, σ of the turn-ons are found to gradually worsen as expected with increasing
 971 pile-up.

972 These features are further emphasised when shown as a function of

$$\frac{(L1 E_T - Offline E_T)}{Offline E_T} \quad (3.4)$$

in bins of matched leading offline jet E_T , of which the individual fits can be found in Appendix (B.2). Each of these distributions are fitted with an EMG function as defined in Equation (3.3).

The μ , σ and λ values extracted for the low, medium and high pile-up conditions are shown for Calo and PF jets in Figure 3.16 and Figure 3.17 respectively. The central value of $\frac{(L1 E_T - \text{Offline } E_T)}{\text{Offline } E_T}$ is observed to increases as a function of jet E_T , whilst the resolution is also observed to improve at higher offline jet E_T .

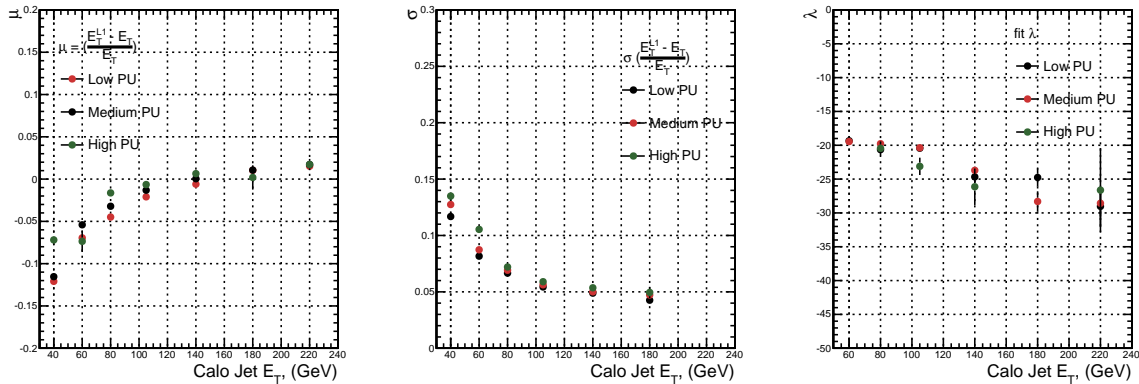


Figure 3.16.: Fit values from an EMG function fitted to the resolution plots of leading Calo jet E_T measured as a function of $\frac{(L1 E_T - \text{Offline } E_T)}{\text{Offline } E_T}$ for low, medium and high pile-up conditions. The plots show the mean μ (left), resolution σ (middle) of the Gaussian as well as the decay term λ (right) of the exponential.

The resolution of other L1 energy sum quantities, H_T , \not{E}_T and $\sum E_T$ parameterised as in Equation (3.4), can be found in Appendix (B.3). The same behaviour observed for the single jet triggers is also found for these quantities, where in the presence of higher pile-up the μ values are shifted to higher values, with a worsening resolution, σ again due to the increase in soft pile-up jets and the absence of pile-up subtraction at L1.

3.4.6. Summary

The performance of the CMS Level-1 Trigger has been studied and evaluated for jets and energy sum quantities using data collected during the 2012 LHC 8TeV run. These studies include the effect of introduction of a 5 GeV jet seed threshold into the jet algorithm configuration, the purpose of which is to mitigate the effects of pile-up on the rate of L1 triggers whilst not adversely affecting the efficiency of these triggers. No significant

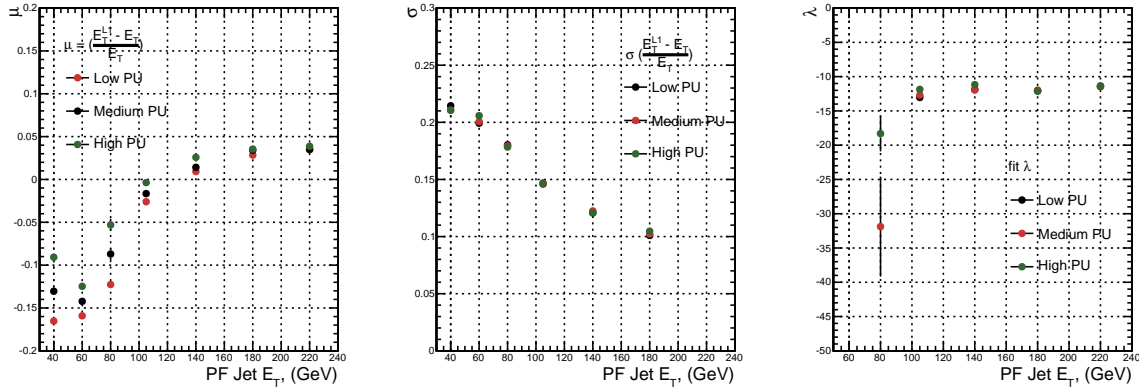


Figure 3.17.: Fit values from an **EMG** function fitted to the resolution plots of leading PF jet E_T measured as a function of $\frac{(L1\ E_T - \text{Offline}\ E_T)}{\text{Offline}\ E_T}$ for low and medium pile-up conditions. The plots show the mean μ (left), resolution σ (middle) of the Gaussian as well as the decay term λ (right) of the exponential.

991 change in performance is observed with this change and good performance is observed
 992 for a range of L1 quantities.

Chapter 4.

993 SUSY searches in Hadronic Final States

995 In this chapter a model independent search for **SUSY** in hadronic final states with \cancel{E}_T
996 using the α_T variable and b-quark multiplicity is introduced and described in detail. The
997 results presented are based on a data sample of pp collisions collected in 2012 at $\sqrt{s} = 8$
998 TeV, corresponding to an integrate luminosity of $11.7 \pm 0.5 \text{ fb}^{-1}$.

999 The kinematic variable α_T is motivated as a variable to provide strong rejections
1000 of QCD backgrounds, whilst maintaining sensitivity to possible a **SUSY** signal within
1001 Section (4.1). The search and trigger strategy in addition to the event reconstruction
1002 and selection are outlined within Sections (4.2-4.2.2).

1003 The method in which the **SM** background is estimated using an analytical technique
1004 to improve statistical precision at higher b-tag multiplicities is detailed within Section
1005 (4.4), with a discussion on the impact of b-tagging and mis-tagging scale factors between
1006 data and MC on any background predictions. Finally a description of the formulation of
1007 appropriate systematic uncertainties applied to the background predictions to account for
1008 theoretical uncertainties and limitations in the simulation modelling of event kinematics
1009 and instrumental effects is covered in Section (4.5).

1010 In addition to the α_T search, a complimentary technique is discussed as a means to
1011 predict the distribution of 3 and 4 reconstructed b-quark jets in an event in Section
1012 (4.6). The recent discovery of the Higgs boson has made third-generation “Natural **SUSY**”
1013 models attractive, given that light top and bottom squarks are a candidate to stabilise
1014 divergent loop corrections to the Higgs boson mass.

1015 Using the α_T search as a base, a simple templated fit is employed to estimate the
 1016 **SM** background in higher b-tag multiplicities (3-4) from a region of a low number
 1017 of reconstructed b-jets (0-2). The predictions using this technique are first tested in
 1018 simulation before being compared to the **SM** background predictions obtained from the
 1019 α_T search.

1020 The experimental reach of the analysis discussed within this thesis is interpreted in
 1021 two classes of **SMS** models, the topologies of which are detailed in Section (2.4.1). The
 1022 **SMS** models considered in this analysis are summaries in Table 4.1. For each model, the
 1023 **LSP** is assumed to be the lightest neutralino.

1024 Within Table 4.1 is also defined reference points, parameterised in terms of parent
 1025 gluino/squark and **LSP** sparticle masses, m_{parent} and m_{LSP} , respectively, which are used
 1026 within the following two chapters to demonstrate potential yields within the signal region
 1027 of the search. The masses are chosen to reflect parameter space which is within the
 1028 expect sensitivity reach of the search.

Model	Production/decay mode	Reference model	
		m_{parent}	m_{LSP}
G1 (T1)	$pp \rightarrow \tilde{g}\tilde{g}^* \rightarrow q\bar{q}\tilde{\chi}_1^0 q\bar{q}\tilde{\chi}_1^0$	700	300
G2 (T1bb)	$pp \rightarrow \tilde{g}\tilde{g}^* \rightarrow b\bar{b}\tilde{\chi}_1^0 b\bar{b}\tilde{\chi}_1^0$	900	500
G3 (T1tt)	$pp \rightarrow \tilde{g}\tilde{g}^* \rightarrow t\bar{t}\tilde{\chi}_1^0 t\bar{t}\tilde{\chi}_1^0$	850	250
D1 (T2)	$pp \rightarrow \tilde{q}\tilde{q}^* \rightarrow q\tilde{\chi}_1^0 \bar{q}\tilde{\chi}_1^0$	600	250
D2 (T2bb)	$pp \rightarrow \tilde{b}\tilde{b}^* \rightarrow b\tilde{\chi}_1^0 \bar{b}\tilde{\chi}_1^0$	500	150
D3 (T2tt)	$pp \rightarrow \tilde{t}\tilde{t}^* \rightarrow t\tilde{\chi}_1^0 \bar{t}\tilde{\chi}_1^0$	400	0

Table 4.1.: A summary of the **SMS** models interpreted in this analysis, involving both direct (D) and gluino-induced (G) production of squarks and their decays. Reference models are also defined in terms of parent and **LSP** sparticle mass

1029 4.1. An introduction to the α_T search

1030 The experimental signature of **SUSY** signal in the hadronic channel would manifest as a
 1031 final state containing energetic jets and \cancel{E}_T . The search focuses on topologies where new
 1032 heavy supersymmetric, R-parity conserving particles are pair-produced in pp collisions.
 1033 These particles decaying to a **LSP** escape the detector undetected, leading to significant
 1034 missing energy and missing hadronic transverse energy,

$$\mathcal{H}_T = \left| \sum_{i=1}^n p_T^{jet_i} \right|, \quad (4.1)$$

1035 defined as the vector sum of the transverse energies of jets selected in an event.
1036 Energetic jets produced in the decay of these supersymmetric particles also can produce
1037 significant visible transverse energy,

$$H_T = \sum_{i=1}^n E_T^{jet_i}, \quad (4.2)$$

1038 defined as the scalar sum of the transverse energies of jets selected in an event.

1039 A search within this channel is greatly complicated in a hadron collider environment,
1040 where the overwhelming background comes from inherently balanced multi-jet (“QCD”)
1041 events which are produced with an extremely large cross section as demonstrated within
1042 Figure 4.1. \cancel{E}_T can appear in such events with a substantial mis-measurement of jet
1043 energy or missed objects due to detector miscalibration or noise effects.

1044 Additional **SM** background from **EWK** processes with genuine \cancel{E}_T from escaping
1045 neutrinos comprise the irreducible background within this search and come mainly from:

- 1046 • $Z \rightarrow \nu\bar{\nu}$ + jets,
- 1047 • $W \rightarrow l\nu$ + jets in which a lepton falls outside of detector acceptance, or the lepton
1048 decays hadronically $\tau \rightarrow \text{had}$,
- 1049 • $t\bar{t}$ with at least one leptonic W decay,
- 1050 • small background contributions from DY, single top and Diboson (WW,ZZ,WZ)
1051 processes.

1052 The search is designed to have a strong separation between events with genuine and
1053 “fake” \cancel{E}_T which is achieved primarily through the dimensionless kinematic variable, α_T
1054 [71][72].

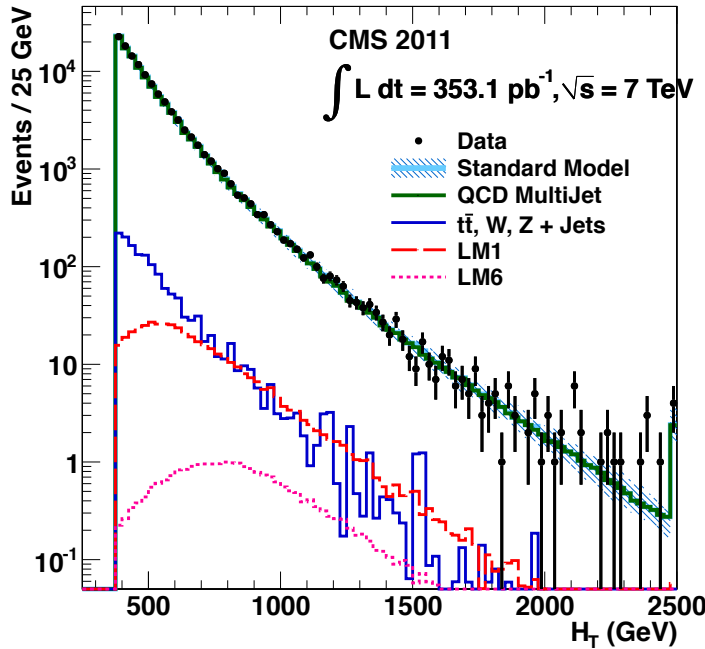


Figure 4.1.: Reconstructed offline H_T for 11.7fb^{-1} of data after a basic pre-selection. Sample is collected from prescaled H_T triggers. Overlaid are expectations from MC simulation of EWK processes as well as a reference signal model (labelled D2 from Table 4.1).

1055 4.1.1. The α_T variable

1056 For a perfectly measured di-jet QCD event, conservation laws dictate that they must be
 1057 produced back-to-back and of equal magnitude. However in di-jet events with real \cancel{E}_T , both of these jets are produced independently of one another, depicted in Figure 4.2.

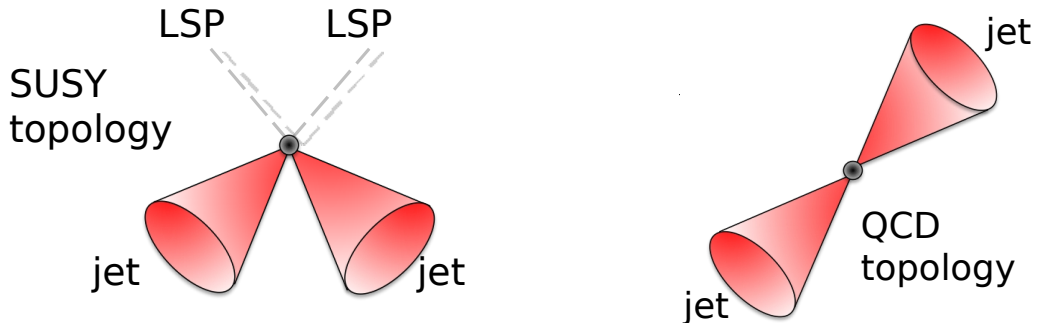


Figure 4.2.: The event topologies of background QCD dijet events (right) and a generic SUSY signature with genuine \cancel{E}_T (left).

1059 Exploiting this feature leads to the formulation of α_T in di-jet systems defined as,

$$\alpha_T = \frac{E_T^{j2}}{M_T}, \quad (4.3)$$

1060 where E_T^{j2} is the transverse energy of the least energetic of the two jets and M_T
1061 defined as:

$$M_T = \sqrt{\left(\sum_{i=1}^2 E_T^{ji}\right)^2 - \left(\sum_{i=1}^2 p_x^{ji}\right)^2 - \left(\sum_{i=1}^2 p_y^{ji}\right)^2} \equiv \sqrt{H_T^2 - \cancel{H}_T^2}. \quad (4.4)$$

1062 A perfectly balanced di-jet event i.e. $E_T^{j1} = E_T^{j2}$ would give an $\alpha_T = 0.5$, where as
1063 events with jets which are not back-to-back, for example in events in which a W or Z
1064 recoils off a system of jets, α_T can achieve values in excess of 0.5.

1065 α_T can be extended to apply to any arbitrary number of jets, undertaken by modelling
1066 a system of n jets as a di-jet system, through the formation of two pseudo-jets [73].
1067 The two pseudo-jets are built by merging the jets present in the event such that the 2
1068 pseudo-jets are chosen to be as balanced as possible, i.e the $\Delta H_T \equiv |E_T^{pj1} - E_T^{pj2}|$ is
1069 minimised between the two pseudo jets. Using Equation (4.4), α_T can be rewritten as,

$$\alpha_T = \frac{1}{2} \frac{H_T - \Delta H_T}{\sqrt{H_T^2 - \cancel{H}_T^2}} = \frac{1}{2} \frac{1 - \Delta H_T/H_T}{\sqrt{1 - (\cancel{H}_T/H_T)^2}}. \quad (4.5)$$

1070 The distribution of α_T for the two jet categories used within this analysis, 2,3 and
1071 ≥ 4 jets, is shown in the Figure 4.3, demonstrating the ability of the α_T variable to
1072 discriminate between multi jet events and EWK processes with genuine \cancel{E}_T in the final
1073 state.

1074 The α_T requirement used within the search is chosen to be $\alpha_T > 0.55$ to ensure
1075 that the QCD multijet background is negligible even in the presence of moderate jet
1076 mis-measurement. There still remains other effects which can cause multijet events to
1077 artificially have a large α_T value, which are discussed in detail in Section (4.2.2).

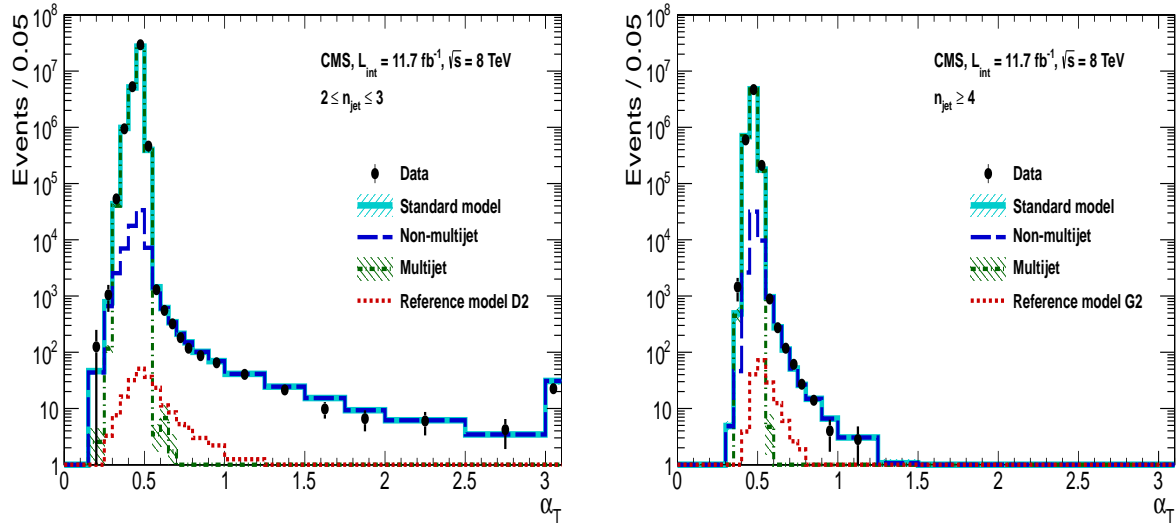


Figure 4.3.: The α_T distributions for the low 2-3 (left) and high ≥ 4 (right) jet multiplicities after a full analysis selection and shown for $H_T > 375$. Data is collected using both prescaled H_T triggers and dedicated α_T triggers for below and above $\alpha_T = 0.55$ respectively. . Expected yields as given by simulation are also shown for multijet events (green dash-dotted line), EWK backgrounds with genuine \cancel{E}_T (blue long-dashed line), the sum of all SM processes (cyan solid line) and the reference signal model D2 (left, red dotted line) or G2 (right, red dotted line).

4.2. Search Strategy

The aim of the analysis presented in this thesis is to identify an excess of events in data over the SM background expectation in multi-jet final states and significant \cancel{E}_T . The essential suppression of the dominant QCD background for such a search is addressed by the α_T variable described in the previous section. For estimation of the remaining EWK backgrounds, three independent data control samples are used to predict the different processes that compose the background :

- $\mu + \text{jets}$ to determine $W + \text{jets}$, $t\bar{t}$ and single top backgrounds,
- $\gamma + \text{jets}$ to determine the irreducible $Z \rightarrow \nu\bar{\nu} + \text{jets}$ background,
- $\mu\mu + \text{jets}$ to determine the irreducible $Z \rightarrow \nu\bar{\nu} + \text{jets}$ background.

These control samples are chosen to both be rich in specific EWK processes, be free of QCD multi-jet events and to also be kinematically similar to the hadronic signal region that they are estimating the backgrounds of, see Section (4.2.3).

1091 To remain inclusive to a large range of possible **SUSY** models, the signal region is
1092 binned in the following categories to allow for increased sensitivity in the interpretation
1093 of results for different **SUSY** topologies:

1094 **Sensitivity to a range of SUSY mass splittings**

1095 The hadronic signal region is defined by $H_T > 275$, divided into eight bins in H_T .

- 1096 – Two bins of width 50 GeV in the range $275 < H_T < 375$ GeV,
1097 – five bins of width 100 GeV in the range $375 < H_T < 875$ GeV,
1098 – and a final open bin, $H_T > 875$ GeV.

1099 The choice at low H_T is driven primarily by trigger constraints. The mass difference
1100 between the **LSP** and the particle that it decays from is an important factor in the
1101 amount of hadronic activity in the event.

1102 A large mass splitting will lead to hard high p_T jets which contribute to the H_T
1103 sum. From Figure 4.1 it can be seen that the **SM** background falls sharply at high
1104 H_T values, therefore a large number of H_T bins will lead to easier identification
1105 of such signals. Conversely smaller mass splittings lead to softer jet p_T 's which will
1106 subsequently fall into the lower H_T range.

1107 **Sensitivity to production method of SUSY particles**

1108 The production mechanism of any potential **SUSY** signal can lead to different event
1109 topologies. One such way to discriminate between gluino ($g\tilde{g}$ - “high multiplicity”),
1110 and direct squark ($q\tilde{q}$ - “low multiplicity”) induced production of **SUSY** particles is
1111 realised through the number of reconstructed jets in the final state.

1112 The analysis is thus split into two jet categories : 2-3 jets , ≥ 4 jets to give sensitivity
1113 to both of these mechanisms.

1114 **Sensitivity to “Natural SUSY” via tagging jets from b-quarks**

1115 Jets originating from bottom quarks (b-jets) are identified through vertices that
1116 are displaced with respect to the primary interaction. The algorithm used to tag
1117 b-jets is the Combined Secondary Vertex Medium Working Point (**CSV**) tagger,
1118 described within Section (3.3.2). A cut is placed on the discriminator variable of
1119 > 0.679 , leading to a gluon/light-quark mis-tag rate of 1% and a jet p_T dependant
1120 b-tagging efficiency of 60-70% [64].

Natural **SUSY** models would be characterised through final-state signatures rich in bottom quarks. A search relying on methods to identify jets originating from bottom quarks through b-tagging, will significantly improve the sensitivity to this class of signature.

This is achieved via the binning of events in the signal region according to the number of b-tagged jets reconstructed in each event, in the following: 0,1,2,3, ≥ 4 b-tag categories . In the highest ≥ 4 b-tag category due to a limited number of expected signal and background, just three H_T bins are employed: 275-325 GeV, 325-375 GeV, ≥ 375 GeV.

This characterisation is identically mirrored in all control samples, with the information from all samples and b-tag categories used simultaneously in the likelihood model (see Chapter 5) in order to interpret the results in a coherent and powerful way.

The combination of the H_T , jet multiplicity and b-tag categorisation of the signal region as described above, resultantly leads to 67 different bins in which the analysis is interpreted in, which is depicted in Figure 4.4.

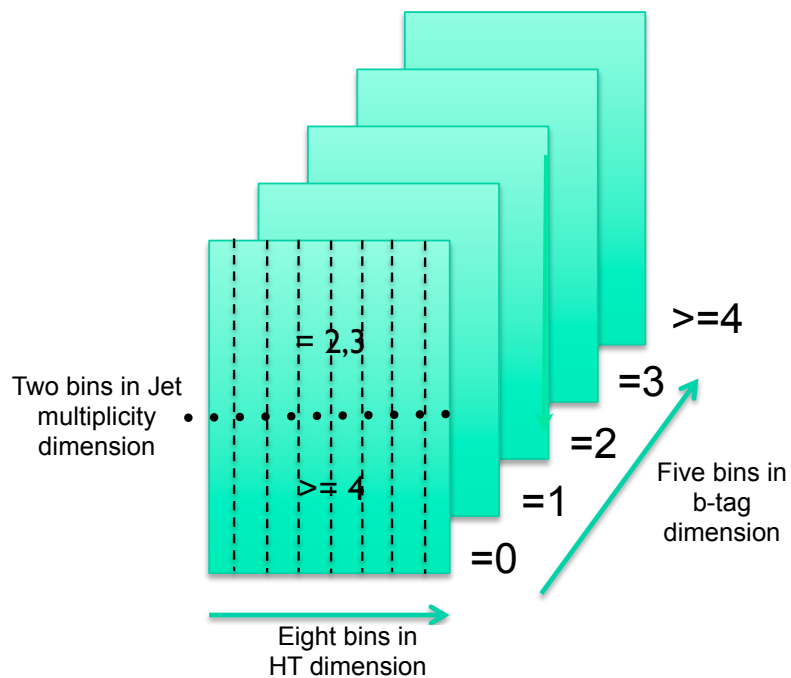


Figure 4.4.: Pictorial depiction of the analysis strategy employed by the α_T search to increase sensitivity to a wide spectra of **SUSY** models.

¹¹³⁷ 4.2.1. Physics Objects

¹¹³⁸ The physics objects used in the analysis defined below, follow the recommendation of
¹¹³⁹ the various CMS Physics Object Groups ([POGs](#)).

¹¹⁴⁰ • Jets

¹¹⁴¹ The jets used in this analysis are CaloJets, reconstructed as described in Section
¹¹⁴² ([3.3.1](#)) using the anti- k_T jet clustering algorithm.

¹¹⁴³ To ensure the jet object falls within the calorimeter systems a pseudo-rapidity
¹¹⁴⁴ requirement of $|\eta| < 3$ is applied. Each jet must pass a “loose” identification criteria
¹¹⁴⁵ to reject jets resulting from unphysical energy, the criteria of which are detailed in
¹¹⁴⁶ Table [4.2](#) [[74](#)].

Variable	Definition
$f_{HPD} < 0.98$	Fraction of jet energy contributed from “hottest” HPD , which rejects HCAL noise.
$f_{EM} > 0.01$	Noise from the HCAL is further suppressed by requiring a minimal electromagnetic component to the jet f_{EM} .
$N_{hits}^{90} \geq 2$	Jets that have $> 90\%$ of its energy from a single channel are rejected, to serve as a safety net that catches jets arising from undiagnosed noisy channels.

Table 4.2.: Jet Identification criteria for the “loose” CaloJet ID, used to reject reconstructed jets resulting from fake calorimeter deposits representing unphysical energy.

¹¹⁴⁷ • Muons

¹¹⁴⁸ Muons are selected in the $\mu +$ jets and $\mu\mu +$ jets control samples, and vetoed in
¹¹⁴⁹ the signal region. The same cut based identification criteria is applied to muons in
¹¹⁵⁰ both search regions and is summarised in Table [4.3](#) [[75](#)].

¹¹⁵¹ Additionally muons are required to be within the acceptance of the muon tracking
¹¹⁵² systems. For the muon control samples, trigger requirements necessitate a $|\eta| <$
¹¹⁵³ 2.1 for the selection of muons. In the signal region where muons are vetoed these
¹¹⁵⁴ conditions are relaxed to $|\eta| < 2.5$ and a minimum threshold of $p_T > 10$ GeV is
¹¹⁵⁵ required of muon objects.

¹¹⁵⁶ • Photons

Categories	Criteria
Global Muon	True
PFMuon	True
χ^2	< 10
Muon chamber hits	> 0
Muon station hits	> 1
Transvere impact d_{xy}	< 0.2mm
Longitudinal distance d_z	< 0.5mm
Pixel hits	> 0
Track layer hits	> 5
PF Isolation (DeltaB corrected)	<0.12

Table 4.3.: Muon Identification criteria used within the analysis for selection/veto purposes in the muon control/signal selections.

1157 Photons are selected within the $\gamma +$ jets control sample and vetoed in all other
1158 selections. Photons are identified in both cases according to the cut based criteria
1159 listed in Table 4.4 [76].

Variable	Definition
$H/E < 0.05$	The ratio of hadronic energy in the HCAL tower directly behind the ECAL super-cluster and the ECAL super-cluster itself.
$\sigma_{in\eta} < 0.011$	The log energy weighted width (σ), of the extent of the shower in the η dimension.
$R9 < 1.0$	The ratio of the energy of the 3×3 crystal core of the super-cluster compared to the total energy stored in the 5×5 super-cluster.
Combined Isolation < 6 GeV	The photons are required to be isolated with no electromagnetic or hadronic activity within a radius $\Delta R = 0.3$ of the photon object. A combination of the pileup subtracted [77], ECAL , HCAL and tracking isolation sums are used to determine the combined total isolation value.

Table 4.4.: Photon Identification criteria used within the analysis for selection/veto purposes in the $\gamma +$ jets control/signal selections.

1160 Photon objects are also required to have a minimum momentum of $p_T > 25$ GeV.

1161 **• Electrons**

1162 Electron identification is defined for veto purposes. They are selected according to
1163 the following cut-based criteria listed in Table 4.5, utilising PF-based isolation.

Categories	Barrel	EndCap
$\Delta\eta_{In}$	0.007	0.009
$\Delta\phi_{In}$	0.15	0.10
$\sigma_{inj\eta}$	0.01	0.03
H/E	0.12	0.10
d0 (vtx)	0.02	0.02
dZ (vtx)	0.20	0.20
$ (1/E_{ECAL} - 1/p_{track}) $	0.05	0.05
PF Combined isolation/ p_T	0.15	0.15
Vertex fit probability	10^{-6}	10^{-6}

Table 4.5.: Electron Identification criteria used within the analysis for veto purposes.

1164 Electrons are required to be identified at $|\eta| < 2.5$, with a minimum $p_T > 10$ GeV
1165 threshold to ensure that the electron falls within the tracking system of the detector.

1166 **• Noise and E_T Filters**

1167 A series of Noise filters are applied to veto events which contain spurious non-physical
1168 jets that are not picked up by the jet id, and events which give large unphysical E_T
1169 values. These filters are listed within Appendix (A.1).

1170 **4.2.2. Event Selection**

1171 The selection criteria for events within the analysis are detailed below. A set of common
1172 cuts are applied to both signal (maximise acceptance to a range of SUSY signatures), and
1173 control samples (retain similar jet kinematics for background predictions), with additional
1174 selection cuts applied to each control sample to enrich the sample in a particular EWK
1175 processes, see Section (4.2.3).

1176 The jets considered in the analysis are required to have a transverse momentum $p_T >$

1177 50 GeV, with a minimum of two jets required in the event. The highest E_T jet is required
1178 to lie within the central tracker acceptance $|\eta| < 2.5$, and the two leading p_T jets must

1179 each have $p_T > 100\text{GeV}$. Any event which has a jet with $p_T > 50\text{ GeV}$ that either fails
1180 the “loose” identification criteria described in Section(4.2.1) or has $|\eta| > 3.0$, is rejected.
1181 Similarly events in which an electron, muon or photon fails object identification but pass
1182 η and p_T restrictions are identified as an “odd” lepton/photon and the event is vetoed.

1183 At low H_T , the jet threshold requirements applied to be considered as part of the
1184 analysis and enter the H_T sum are scaled downwards. These are scaled down in order to
1185 not restrict phase space, preserving jet multiplicities and background admixture in the
1186 lower H_T bins, as listed in Table 4.6.

H_T bin	minimum jet p_T	second leading jet p_T
$275 < H_T < 325$	36.7	73.3
$325 < H_T < 375$	43.3	86.6
$375 < H_T$	50.0	100.0

Table 4.6.: Jet thresholds used in the three H_T regions of the analysis.

1177 Within the signal region to suppress **SM** processes with genuine \cancel{E}_T from neutrinos,
1188 events containing isolated electrons or muons are vetoed. Furthermore to ensure a pure
1189 multi-jet topology, events are vetoed if an isolated photon is found with $p_T > 25\text{ GeV}$.

1190 An α_T requirement of > 0.55 is required to reduce the QCD multi-jet background
1191 to a negligible amount. Finally additional cleaning cuts are applied to protect against
1192 pathological deficiencies such as reconstruction failures or severe energy mis-measurements
1193 due to detector inefficiencies:

- Significant H_T can arise in events with no real \cancel{E}_T due to multiple jets falling below the p_T threshold used for selecting jets. This in turn leads to events which can then incorrectly pass the α_T requirements of the analysis. This effect can be negated by requiring that the missing transverse momentum reconstructed from jets alone does not greatly exceed the missing transverse momentum reconstructed from all of the detector’s calorimeter towers,

$$H_T/\cancel{E}_T < 1.25.$$

- 1194 • Fake \cancel{E}_T and H_T can arise due to significant jet mis-measurements cause by a small
1195 number of non-functioning **ECAL** regions. These regions absorb electromagnetic
1196 showers which are subsequently not added to the jet energy sum. To circumvent

1197 this problem the following procedure is employed : For each jet in the event, the
1198 angular separation

$$\Delta\phi_j^* \equiv \Delta\phi(p_j^\rightarrow - \sum_{i \neq j} p_i^\rightarrow), \quad (4.6)$$

1199 is calculated where that jet is itself removed from the event. Here $\Delta\phi^*$ is a measure
1200 of how aligned the H_T of an event is with a jet, a small value is compatible with the
1201 hypothesis of an inherently balanced event in which a jet has been mis-measured.
1202 For every jet in a event with $\Delta\phi^* < 0.5$, if the ΔR distance between the selected jet
1203 and the closest dead **ECAL** region is also < 0.3 , then the event is rejected. Similarly
1204 events are rejected if the jet points within $\Delta R < 0.3$ of the **ECAL** barrel-endcap
1205 gap at $|\eta| = 1.5$.

1206 Some of the key distributions of the data used in this analysis compared to MC
1207 simulation are shown in Figure !!!.. The MC samples are normalised to a luminosity
1208 of 11.7 fb^{-1} , split into the jet categories used within the analysis, with no requirement
1209 placed upon the number of b-tagged jets in the events.

1210 The distributions shown are presented for purely illustrative purposes, with the MC
1211 simulation itself not used in absolute term to estimate the yields from background
1212 processes, see Sections (4.2.3,4.4). However it is nevertheless important to demonstrate
1213 that good agreement exists between simulation and observation in data.

1214 PUT PLOTS HERE

1215 4.2.3. Control Sample Definition

1216 The method used to estimate the background contributions in the hadronic signal region
1217 relies on the use of a Transfer Factor (**TF**). This is determined from MC simulation
1218 in both the control, $N_{\text{MC}}^{\text{control}}$, and signal, $N_{\text{MC}}^{\text{signal}}$, region to transform the observed yield
1219 measured in data for a control sample, $N_{\text{obs}}^{\text{control}}$, into a background prediction, $N_{\text{pred}}^{\text{signal}}$, via
1220 Equation (4.7),

$$N_{\text{pred}}^{\text{signal}} = \frac{N_{\text{MC}}^{\text{signal}}}{N_{\text{MC}}^{\text{control}}} \times N_{\text{obs}}^{\text{control}}. \quad (4.7)$$

All MC samples are normalised to the luminosity of the data samples, 11.7 fb^{-1} .

Through this method, “vanilla” predictions for the SM background in the signal region can be made by considering separately the sum of the prediction from either the $\mu + \text{jets}$ and $\gamma + \text{jets}$ or $\mu + \text{jets}$ and $\mu\mu + \text{jets}$ samples. However the final background estimation from which results are interpreted, is calculated via a fitting procedure defined formally by the likelihood model described in Chapter 5.

The control samples and the EWK processes they are specifically tuned to select are

defined below:

The $\mu + \text{jets}$ control sample

Events from $W + \text{jets}$ and $t\bar{t}$ processes enter into the hadronic signal sample due to unidentified leptons from acceptance or threshold effects and hadronic tau decays. These leptons originate from the decay of high p_T W bosons.

The control samples specifically identifies $W \rightarrow \mu\bar{\nu}$ decays within the same phase-space of the signal region, where the muon is subsequently ignored in the calculation of event level variables, i.e. H_T , \mathcal{H}_T , α_T . All kinematic jet-based cuts are identical to those applied in the hadronic search region detailed in Section (4.2.2), with the same H_T , jet multiplicity and b-jet multiplicity binning described above.

- Muons originating from W boson decays are selected by requiring one tightly isolated muon defined in Table 4.3, with a $p_T > 30 \text{ GeV}$ and $|\eta| < 2.1$. Both of these threshold arise from trigger restrictions.
- The transverse mass of the W candidate must satisfy $M_T(\mu, \cancel{E}_T) < 30 \text{ GeV}$ (to suppress QCD multi-jet events).
- Events which contain a jet overlapping with a muon $\Delta R(\mu, \text{jet}) < 0.5$ are vetoed to remove events from muons produced as part of a jet’s hadronisation process.
- Events containing a second muon candidate which has failed id, but passed p_T and $|\eta|$ requirements, are checked to have an invariant mass that satisfies $m_Z - 25 < M_{\mu_1\mu_2} > m_Z + 25$, thus removing $Z \rightarrow \mu\mu$ contamination.

1248 The $\mu\mu + \text{jets}$ control sample

1249 The $Z \rightarrow \nu\bar{\nu} + \text{jets}$ background enters into the signal region from genuine E_T from
1250 the escaping neutrinos. This background is estimated using two control samples,
1251 the first of which is the $Z \rightarrow \mu\bar{\mu} + \text{jets}$ process, which posses identical kinematic
1252 properties, but with different acceptance and branching ratio [1].

1253 The same acceptance requirements as the $\mu + \text{jets}$ selection for muons is applied,
1254 as defined in Table 4.3. Muons in the event are ignored for the purpose of the
1255 calculation of event level variables. Kinematic jet-based cuts and phase space
1256 binning identical to the hadronic search region are also applied.

- 1257 – Muons origination from a Z boson decay are selected requiring exactly two
1258 tightly isolated muons. Due to trigger requirements the leading muon is required
1259 to have $p_T > 30$ GeV and $|\eta| < 2.1$. The requirement of the p_T on the second
1260 muon is relaxed to 10 GeV.
- 1261 – Events are vetoed if containing a jet overlapping with a muon $\Delta R(\mu, \text{jet}) < 0.5$.
- 1262 – In order to specifically select two muons both originating from a single Z boson
1263 decay, the invariant mass of the two muons must satisfy $m_Z - 25 > M_{\mu_1\mu_2} <$
1264 $m_Z + 25$.

1265 The $\mu\mu + \text{jets}$ sample is used to make predictions in the signal region in the two
1266 lowest H_T bins, providing coverage where the $\gamma + \text{jets}$ sample is unable to, due to
1267 trigger requirements. In higher H_T bins, the higher statistics of the $\gamma + \text{jets}$ sample
1268 is instead used to determine the $Z \rightarrow \nu\bar{\nu}$ estimation.

1269 The $\gamma + \text{jets}$ control sample

1270 The $Z \rightarrow \nu\bar{\nu} + \text{jets}$ background is also estimated from a $\gamma + \text{jets}$ control sample,
1271 which possesses a larger cross section and kinematic properties similar to those of
1272 $Z \rightarrow \mu\bar{\mu}$ events where the photon is ignored [78][79]. The photon is ignored for the
1273 purpose of the calculation of event level variables, and identical selection cuts to
1274 the hadronic signal region are applied.

- 1275 – Exactly one photon is selected, satisfying identification criteria as detailed in
1276 Table 4.4, with a minimum $p_T > 165$ GeV to satisfy trigger thresholds and $|\eta|$
1277 < 1.45 to ensure the photon remains in the barrel of the detector.

- 1278 – A selection criteria of $\Delta R(\gamma, jet) < 1.0$, between the photon and all jets is
1279 applied to ensure the acceptance of only well isolated $\gamma +$ jets events.
- 1280 – Given that the photon is ignored, this control sample can only be applied in
1281 the H_T region > 375 GeV, due to the trigger thresholds on the minimum p_T of
1282 the photon, and the requirement of an $\alpha_T > 0.55$ cut.

1283 The sum of the expected yields from all MC samples, in each control sample enter
1284 the denominator, N_{MC}^{control} , of the **TF** defined in Eq (4.7). However for the numerator ,
1285 N_{MC}^{signal} , only the relevant processes that the control sample is estimating a background
1286 for, enter into the **TF**.

1287 For the $\mu +$ jets sample the simulated MC processes which enter the numerator of
1288 the **TF** are,

$$N_{MC}^{\text{signal}}(H_T, n_{\text{jet}}) = N_W + N_{t\bar{t}} + N_{DY} + N_t + N_{di-boson}, \quad (4.8)$$

1289 whilst for both the $\mu\mu +$ jets and $\gamma +$ jets samples the only MC process used in the
1290 numerator is,

$$N_{MC}^{\text{signal}}(H_T, n_{\text{jet}}) = N_{Z \rightarrow \nu\bar{\nu}}. \quad (4.9)$$

1291 The selection criteria of the three control samples are defined to ensure background
1292 composition and event kinematics mirror closely the signal region. This is done in order
1293 to minimise the reliance on MC simulation to model correctly the backgrounds and event
1294 kinematics in the control and signal samples. However.. The α_T requirement is relaxed.

1295 Put sample distributions here

₁₂₉₆ **4.3. Trigger Strategy**

₁₂₉₇ **4.4. A method to determine MC yields with higher
statistical precision**

₁₂₉₉ **4.5. Systematic Uncertainties on Transfer Factors**

₁₃₀₀ **4.6. Searches for Natural SUSY with B-tag
templates.**

₁₃₀₂ Btag Templates blah blah

Chapter 5.

¹³⁰³ Results

¹³⁰⁴ Results at 12fb 8TeV

¹³⁰⁵ 5.1. Statistical Interpretation

¹³⁰⁶ Likelihood stuff

¹³⁰⁷ 5.2. Interpretation in Simplified Signal Models

¹³⁰⁸ Result interpretation

¹³⁰⁹

Appendix A.

¹³¹⁰ **Miscellaneous**

¹³¹¹ **A.1. Noise Filters**

¹³¹² For Calo jets the following criteria were applied:

¹³¹³ • N90 hits > 1 ,

¹³¹⁴ • HBHE > 0.01 ,

¹³¹⁵ • fHPD < 0.98 ,

¹³¹⁶ For PF jets the following criteria were applied:

¹³¹⁷ • Neutral hadron fraction < 0.99 ,

¹³¹⁸ • Neutral EM fraction < 0.99 ,

¹³¹⁹ • Number of constituents > 1 ,

¹³²⁰ • Charged hadron fraction > 0 ,

¹³²¹ • Charged multiplicity > 0 ,

¹³²² • Charged EM fraction < 0.99 .

¹³²³ The following noise filters are applied, to remove events with spurious, non-physical
¹³²⁴ jets or missing transverse energy.

¹³²⁵ • CSC tight beam halo filter,

¹³²⁶ • HBHE noise filter with isolated noise rejection,

- 1327 • HCAL laser filter,
- 1328 • ECAL dead cell trigger primitive (TP) filter,
- 1329 • Tracking failure filter,
- 1330 • Bad EE Supercrystal filter,
- 1331 • ECAL Laser correction filter.

1332 A.2. Primary Vertices

1333 The pileup per event is defined by the number of 'good' reconstructed primary vertices
1334 in the event, with each vertex satisfying the following requirements

- 1335 • $N_{dof} > 4$;
- 1336 • vertex position along the bead direction of $|z_{vtx}| < 24\text{cm}$;
- 1337 • vertex position perpendicular to the beam of $\rho < 2\text{cm}$.

Appendix B.

¹³³⁸ L1 Jets

¹³³⁹ B.1. Jet matching efficiencies

¹³⁴⁰ The single jet turn-on curves are derived from events independent of whether the leading
¹³⁴¹ jet in an event is matched to a Level 1 jet using ΔR matching detailed in Section (3.4.3)
¹³⁴² or not. These turn-ons are produced from events which are not triggered on jet quantities
¹³⁴³ and therefore it is not guaranteed that the lead jet of an event will be seeded by a Level
¹³⁴⁴ 1 jet. Figure B.1 shows the particular matching efficiency of a lead jet to a L1 jet.

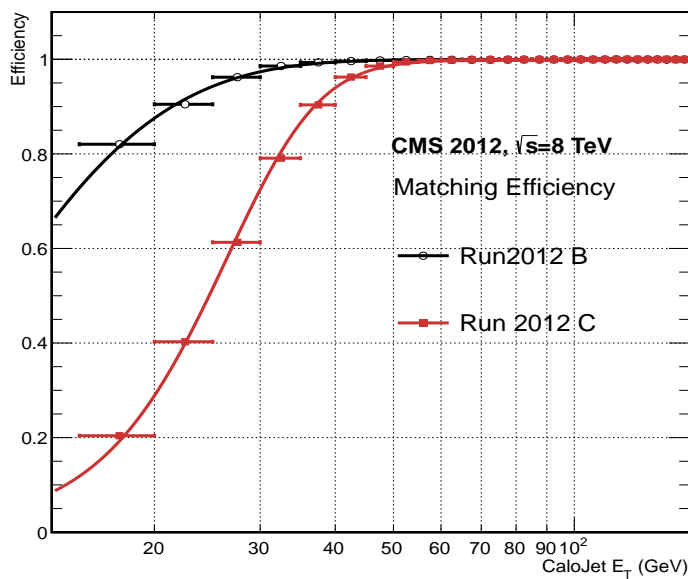


Figure B.1.: Leading jet matching efficiency as a function of the offline CaloJet E_T , measured in an isolated muon triggered dataset in the 2012B and 2012C run periods.

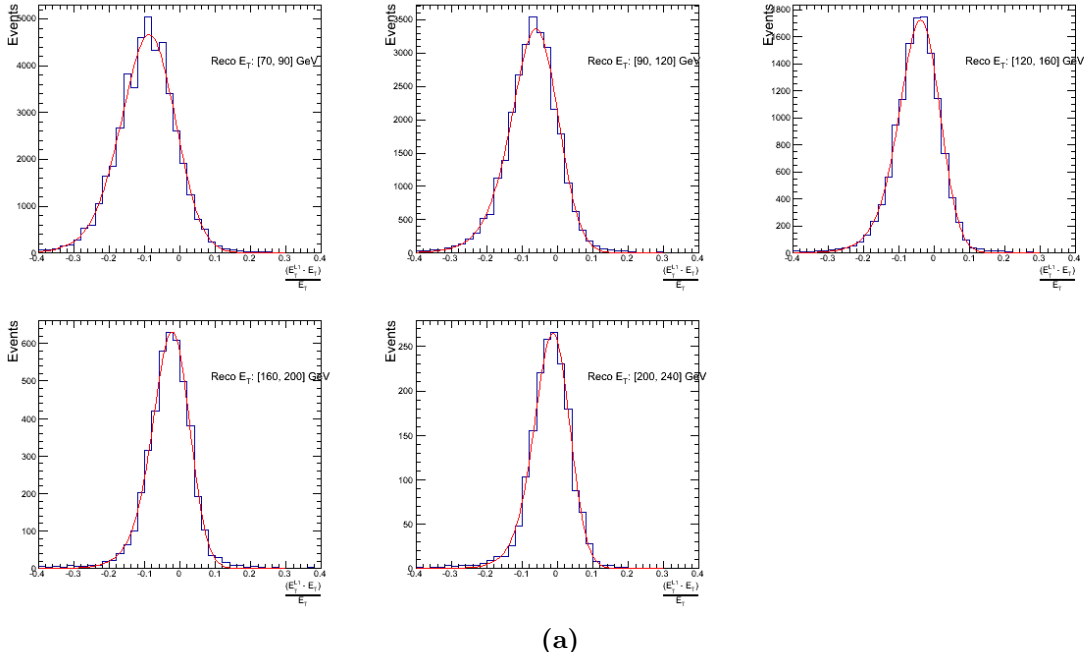
Run Period	μ	σ
2012B	6.62 ± 0.01	0.79 ± 0.03
2012C	19.51 ± 0.03	7.14 ± 0.02

Table B.1.: Results of a cumulative EMG function fit to the turn-on curves for the matching efficiency of the leading jet in an event to a Level-1 jet in run 2012C and 2012B data, measured in an isolated muon triggered sample. The turn-on point, μ , and resolution, σ , are measured with respect to offline Calo Jet E_T .

It can be seen that the turn on is sharper during the 2012B run period. The seed threshold requirement of a 5 GeV jet seed in run 2012C results in more events in which even the lead offline jet does not have an associated L1 jet. For larger jet E_T thresholds, typical of thresholds used in physics analyses, 100% efficiency is observed.

The matching efficiencies have a μ values of 6.62 GeV and 19.51 GeV for Run 2012B and 2012C respectively and is shown in Table B.1.

B.2. Leading Jet Energy Resolution



(a)

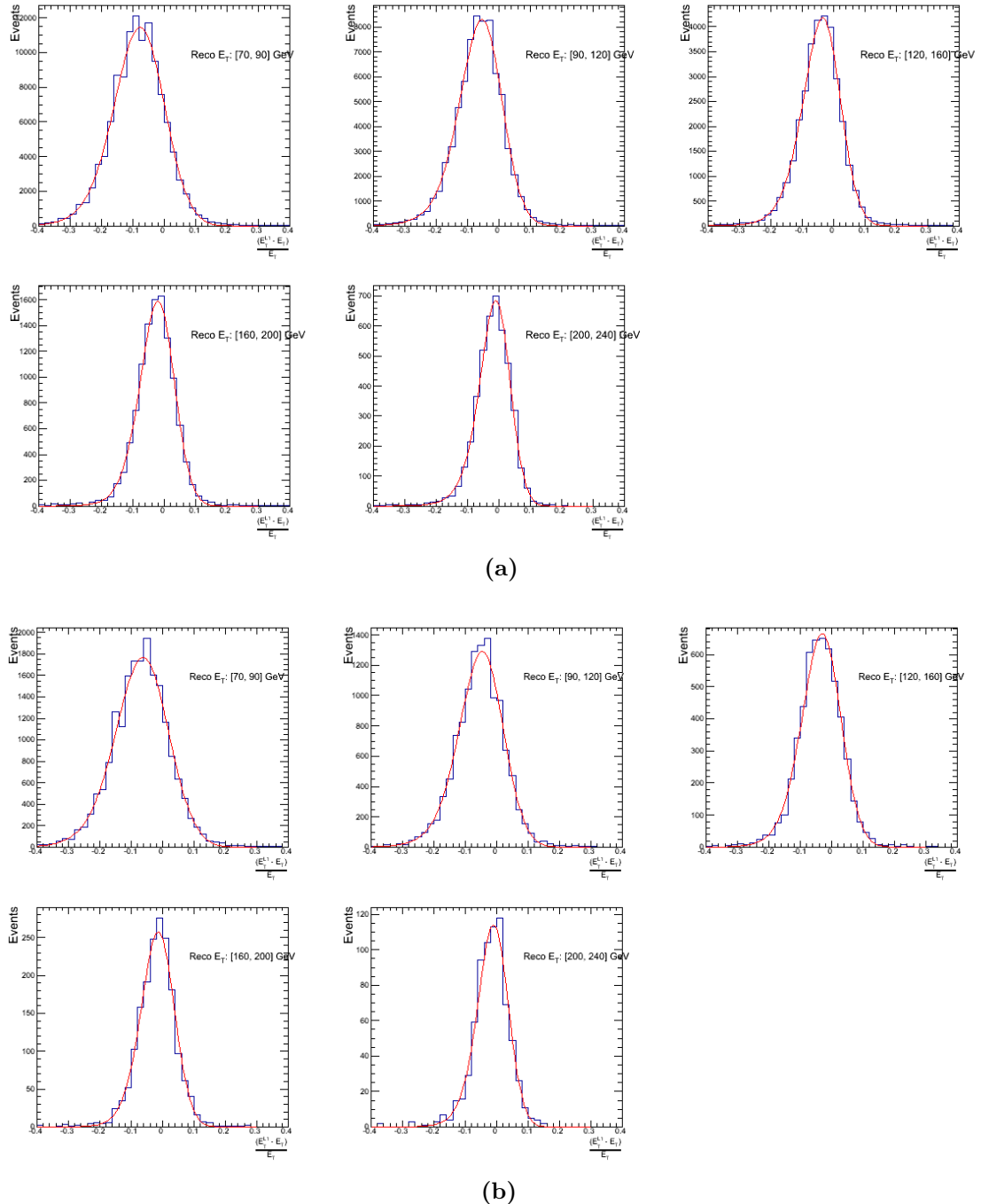
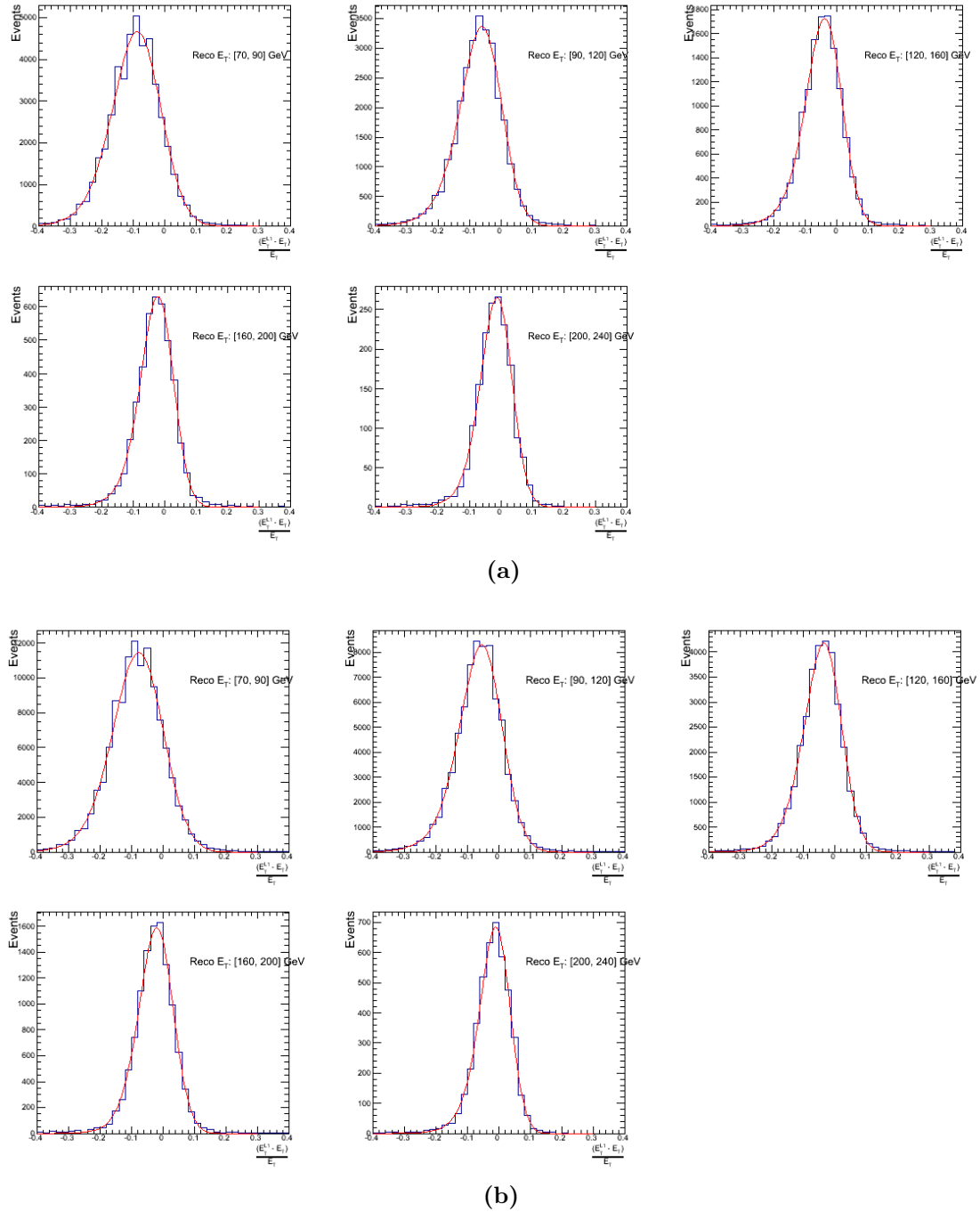
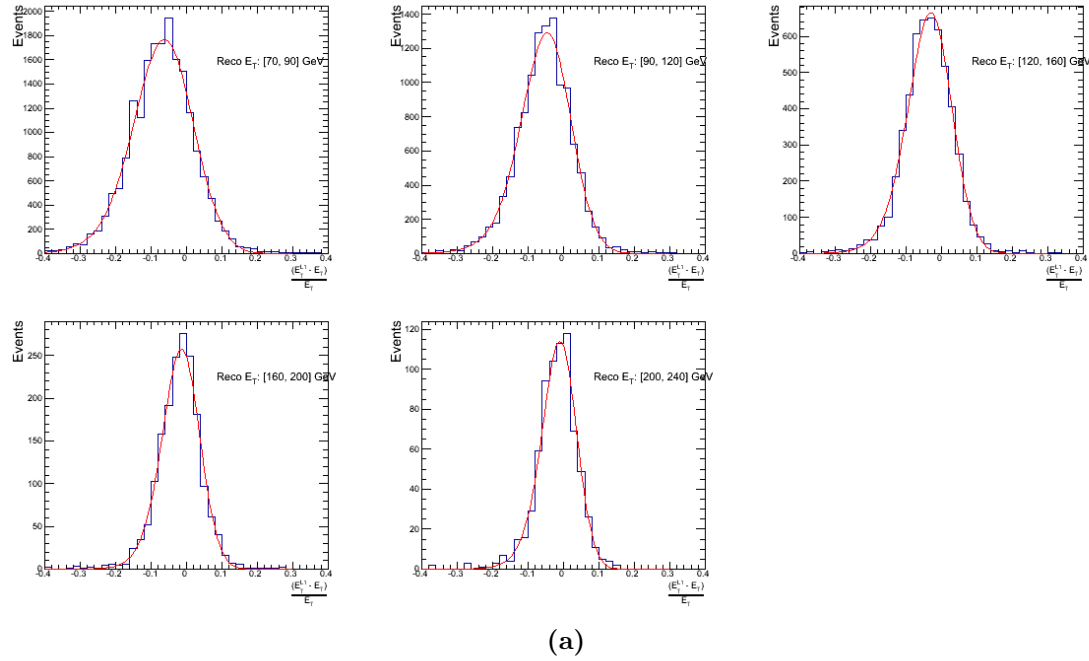


Figure B.2.: Resolution plots of the leading offline jet Calo E_T measured as a function of $\frac{(\text{L1 } E_T - \text{Offline } E_T)}{\text{Offline } E_T}$ for low (a), medium (b) and high (c) pile-up conditions.





(a)

Figure B.3.: Resolution plots of the leading offline jet PF E_T measured as a function of $\frac{(L1 E_T - Offline E_T)}{Offline E_T}$ for low (a), medium (b) and high (c) pile-up conditions.

1352 B.3. Resolution for Energy Sum Quantities

1353 The following plots show the resolution parameters for the four energy sum quantities as
 1354 a function of the quantity (q) itself. In this case, The mean and RMS of the individual
 1355 $\frac{(L1 q - Offline q)}{Offline q}$ distributions, in bins of the quantity q is displayed.

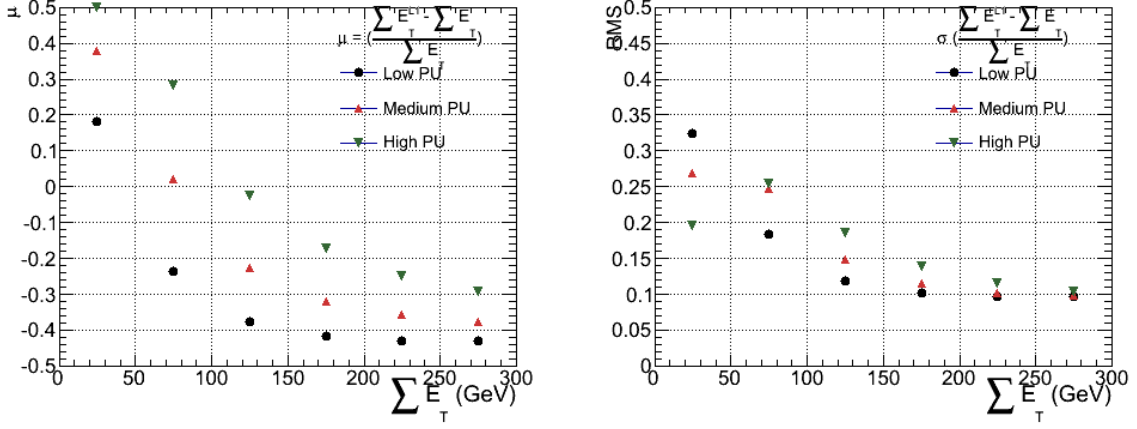


Figure B.4.: $\sum E_T$ resolution parameters in bins of Calo $\sum E_T$ measured for the defined low, medium and high pile up conditions. The plots show the mean μ (left), resolution σ (RMS) of the $\frac{\Delta q}{q}$ distributions.

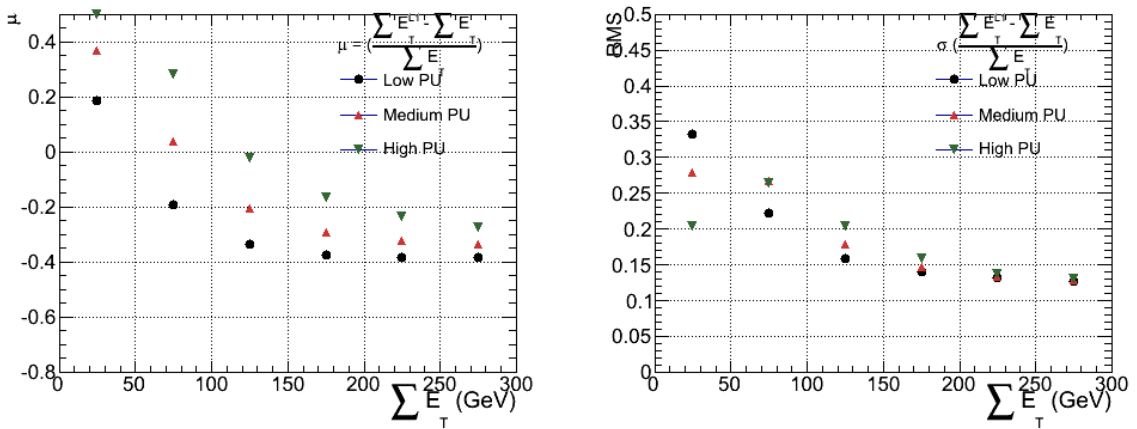


Figure B.5.: $\sum E_T$ resolution parameters in bins of PF $\sum E_T$ measured for the defined low, medium and high pile up conditions. The plots show the mean μ (left), resolution σ (RMS) of the $\frac{\Delta q}{q}$ distributions.

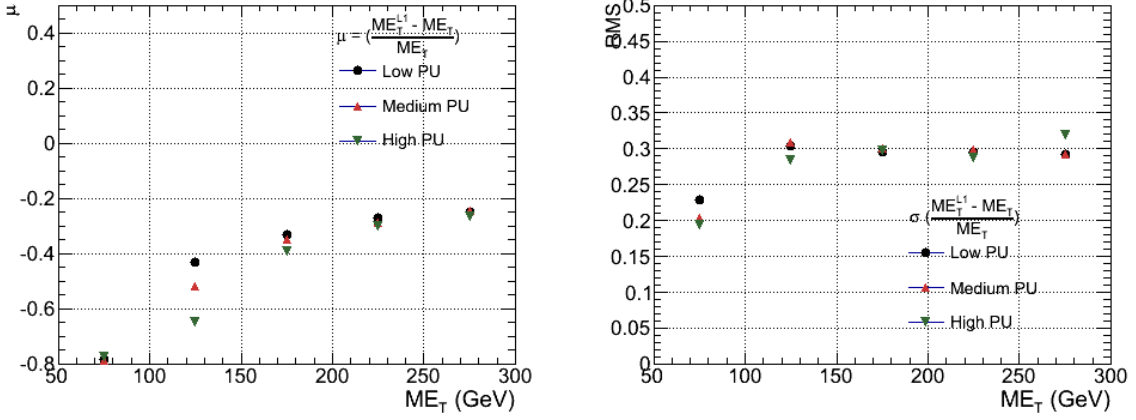


Figure B.6.: \mathcal{E}_T resolution parameters in bins of Calo \mathcal{E}_T measured for the defined low, medium and high pile up conditions. The plots show the mean μ (left), resolution σ (RMS) of the $\frac{\Delta q}{q}$ distributions.

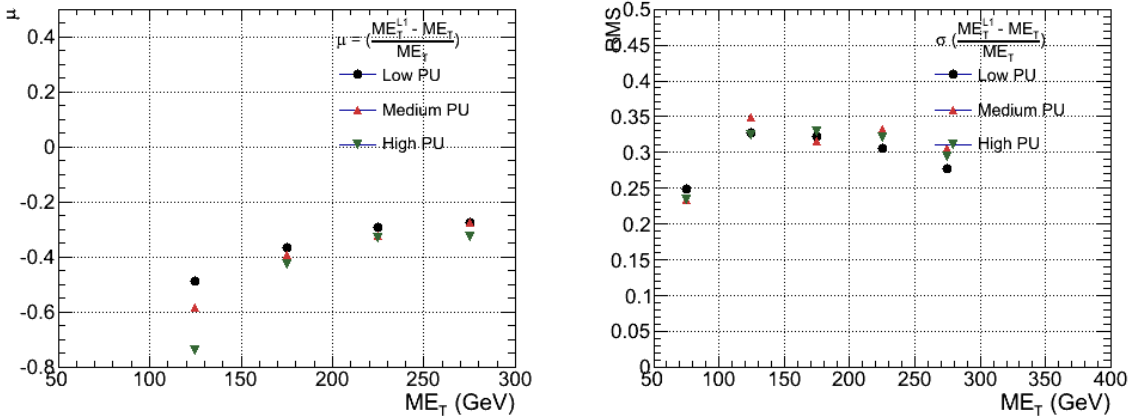


Figure B.7.: \mathcal{E}_T resolution parameters in bins of PF \mathcal{E}_T measured for the defined low, medium and high pile up conditions. The plots show the mean μ (left), resolution σ (RMS) of the $\frac{\Delta q}{q}$ distributions.

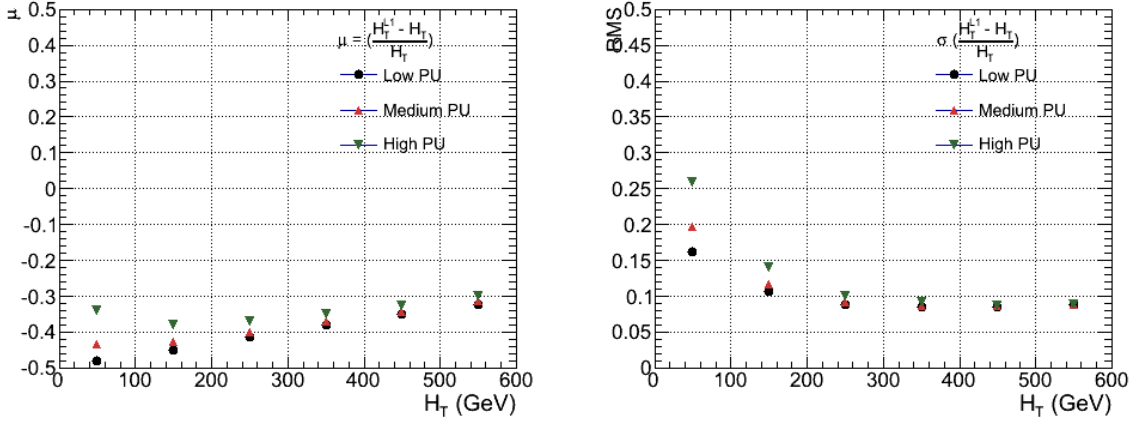


Figure B.8.: H_T resolution parameters in bins of Calo H_T measured for the defined low, medium and high pile up conditions. The plots show the mean μ (left), resolution σ (RMS) of the $\frac{\Delta q}{q}$ distributions.

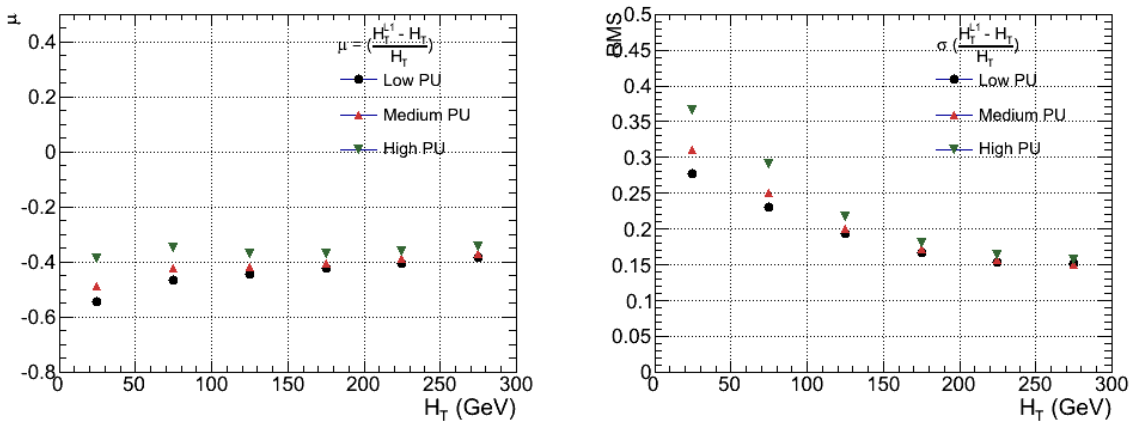


Figure B.9.: H_T resolution parameters in bins of PF H_T measured for the defined low, medium and high pile up conditions. The plots show the mean μ (left), resolution σ (RMS) of the $\frac{\Delta q}{q}$ distributions.

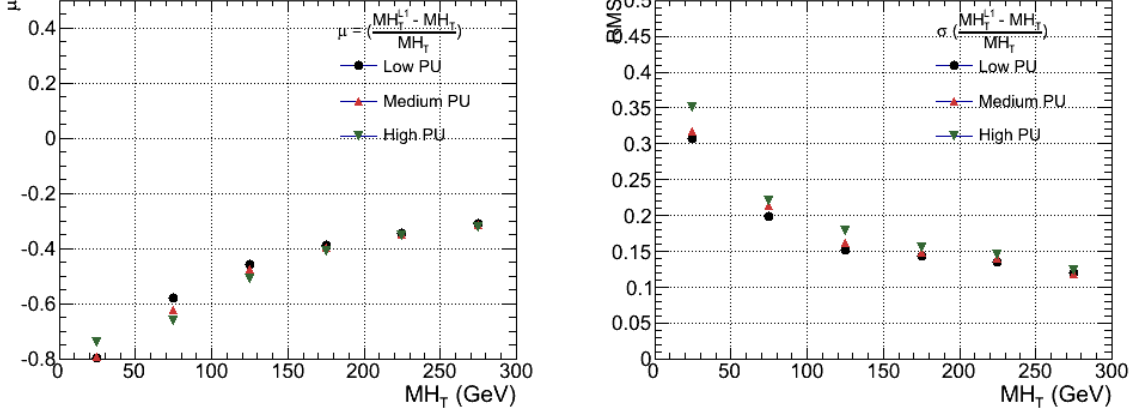


Figure B.10.: H_T resolution parameters in bins of H_T measured for the defined low, medium and high pile up conditions. The plots show the mean μ (left), resolution σ (RMS) of the $\frac{\Delta q}{q}$ distributions.

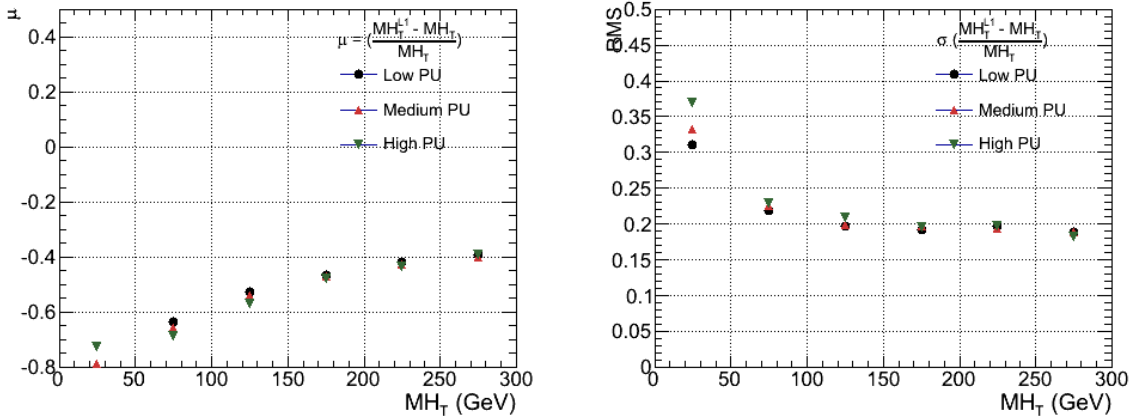


Figure B.11.: H_T resolution parameters in bins of PF H_T measured for the defined low, medium and high pile up conditions. The plots show the mean μ (left), resolution σ (RMS) of the $\frac{\Delta q}{q}$ distributions.

¹³⁵⁷ Bibliography

- ¹³⁵⁸ [1] J. Beringer *et al.*, “Review of Particle Physics (RPP),” *Phys.Rev.*, vol. D86, p. 010001, 2012.
- ¹³⁶⁰ [2] G. H. et al., “Nine-year wilkinson microwave anisotropy probe (wmap) observations: Cosmological parameter results,” *The Astrophysical Journal Supplement Series*, vol. 208, no. 2, p. 19, 2013.
- ¹³⁶³ [3] G. Aad *et al.*, “Observation of a new particle in the search for the Standard Model Higgs boson with the ATLAS detector at the LHC,” *Phys.Lett.*, vol. B716, pp. 1–29, 2012.
- ¹³⁶⁶ [4] S. Chatrchyan *et al.*, “Observation of a new boson at a mass of 125 GeV with the CMS experiment at the LHC,” *Phys.Lett.*, vol. B716, pp. 30–61, 2012.
- ¹³⁶⁸ [5] S. Chatrchyan *et al.*, “Search for supersymmetry in hadronic final states with missing transverse energy using the variables AlphaT and b-quark multiplicity in pp collisions at 8 TeV,” *Eur.Phys.J.*, vol. C73, p. 2568, 2013.
- ¹³⁷¹ [6] S. Weinberg, “A model of leptons,” *Phys. Rev. Lett.*, vol. 19, pp. 1264–1266, Nov 1967.
- ¹³⁷³ [7] S. Glashow, “Partial Symmetries of Weak Interactions,” *Nucl.Phys.*, vol. 22, pp. 579–588, 1961.
- ¹³⁷⁵ [8] A. Salam, “Weak and Electromagnetic Interactions,” *Conf.Proc.*, vol. C680519, pp. 367–377, 1968.
- ¹³⁷⁷ [9] G. Hooft, “Renormalizable lagrangians for massive yang-mills fields,” *Nuclear Physics B*, vol. 35, no. 1, pp. 167 – 188, 1971.
- ¹³⁷⁹ [10] F. Hasert *et al.*, “Observation of Neutrino Like Interactions Without Muon Or Electron in the Gargamelle Neutrino Experiment,” *Phys.Lett.*, vol. B46, pp. 138–140, 1973.

- [11] G. Arnison *et al.*, “Experimental Observation of Lepton Pairs of Invariant Mass Around 95-GeV/c**2 at the CERN SPS Collider,” *Phys.Lett.*, vol. B126, pp. 398–410, 1983.
- [12] M. Banner *et al.*, “Observation of Single Isolated Electrons of High Transverse Momentum in Events with Missing Transverse Energy at the CERN anti-p p Collider,” *Phys.Lett.*, vol. B122, pp. 476–485, 1983.
- [13] E. Noether, “Invariante variationsprobleme,” *Nachrichten von der Gesellschaft der Wissenschaften zu Gttingen, Mathematisch-Physikalische Klasse*, vol. 1918, pp. 235–257, 1918.
- [14] F. Halzen and A. D. Martin, “Quarks and leptons.” Wiley, 1985.
- [15] *Introduction to Elementary Particles*. Wiley-VCH, 2nd ed., Oct. 2008.
- [16] C. S. Wu, E. Ambler, R. W. Hayward, D. D. Hoppes, and R. P. Hudson, “Experimental Test of Parity Conservation in Beta Decay,” *Physical Review*, vol. 105, pp. 1413–1415, Feb. 1957.
- [17] P. Higgs, “Broken symmetries, massless particles and gauge fields,” *Physics Letters*, vol. 12, no. 2, pp. 132 – 133, 1964.
- [18] F. Englert and R. Brout, “Broken symmetry and the mass of gauge vector mesons,” *Phys. Rev. Lett.*, vol. 13, pp. 321–323, Aug 1964.
- [19] P. W. Higgs, “Broken symmetries and the masses of gauge bosons,” *Phys. Rev. Lett.*, vol. 13, pp. 508–509, Oct 1964.
- [20] G. S. Guralnik, C. R. Hagen, and T. W. B. Kibble, “Global conservation laws and massless particles,” *Phys. Rev. Lett.*, vol. 13, pp. 585–587, Nov 1964.
- [21] S. Weinberg, “A model of leptons,” *Phys. Rev. Lett.*, vol. 19, pp. 1264–1266, Nov 1967.
- [22] H. Yukawa, “On the interaction of elementary particles. i,” *Progress of Theoretical Physics Supplement*, vol. 1, pp. 1–10, 1955.
- [23] Y. e. a. Fukuda, “Evidence for oscillation of atmospheric neutrinos,” *Phys. Rev. Lett.*, vol. 81, pp. 1562–1567, Aug 1998.
- [24] R. Becker-Szendy, C. Bratton, D. Casper, S. Dye, W. Gajewski, *et al.*, “A Search for muon-neutrino oscillations with the IMB detector,” *Phys.Rev.Lett.*, vol. 69,

- ¹⁴¹² pp. 1010–1013, 1992.
- ¹⁴¹³ [25] S. P. Martin, “A Supersymmetry primer,” 1997.
- ¹⁴¹⁴ [26] H. Nilles, *Supersymmetry, Supergravity and Particle Physics*. Physics reports, North-Holland Physics Publ., 1984.
- ¹⁴¹⁵
- ¹⁴¹⁶ [27] H. E. Haber and G. L. Kane, “The Search for Supersymmetry: Probing Physics Beyond the Standard Model,” *Phys.Rept.*, vol. 117, pp. 75–263, 1985.
- ¹⁴¹⁷
- ¹⁴¹⁸ [28] E. Witten, “Dynamical Breaking of Supersymmetry,” *Nucl.Phys.*, vol. B188, p. 513, 1981.
- ¹⁴¹⁹
- ¹⁴²⁰ [29] J. Wess and B. Zumino, “Supergauge transformations in four dimensions,” *Nuclear Physics B*, vol. 70, no. 1, pp. 39 – 50, 1974.
- ¹⁴²¹
- ¹⁴²² [30] H. Muller-Kirsten and A. Wiedemann, *Introduction to Supersymmetry*. World Scientific lecture notes in physics, World Scientific, 2010.
- ¹⁴²³
- ¹⁴²⁴ [31] I. Aitchison, *Supersymmetry in Particle Physics: An Elementary Introduction*. Cambridge University Press, 2007.
- ¹⁴²⁵
- ¹⁴²⁶ [32] K. A. Intriligator and N. Seiberg, “Lectures on Supersymmetry Breaking,” *Class.Quant.Grav.*, vol. 24, pp. S741–S772, 2007.
- ¹⁴²⁷
- ¹⁴²⁸ [33] Y. Shadmi, “Supersymmetry breaking,” pp. 147–180, 2006.
- ¹⁴²⁹
- ¹⁴³⁰ [34] C. Burgess, P. G. Camara, S. de Alwis, S. Giddings, A. Maharana, *et al.*, “Warped Supersymmetry Breaking,” *JHEP*, vol. 0804, p. 053, 2008.
- ¹⁴³¹
- ¹⁴³² [35] H. Murayama, “Supersymmetry breaking made easy, viable, and generic,” 2007.
- ¹⁴³³
- ¹⁴³⁴ [36] H. Baer and X. Tata, *Weak Scale Supersymmetry: From Superfields to Scattering Events*. Cambridge University Press, 2006.
- ¹⁴³⁵
- ¹⁴³⁶ [37] S. P. Martin, “Implications of supersymmetric models with natural r-parity conservation,” 1996.
- ¹⁴³⁷
- ¹⁴³⁸ [38] G. L. Kane, C. F. Kolda, L. Roszkowski, and J. D. Wells, “Study of constrained minimal supersymmetry,” *Phys.Rev.*, vol. D49, pp. 6173–6210, 1994.
- ¹⁴³⁹
- ¹⁴⁴⁰ [39] C. Stlege, G. Bertone, D. Cerdeno, M. Fornasa, R. Ruiz de Austri, *et al.*, “Updated global fits of the cmSSM including the latest LHC SUSY and Higgs searches and XENON100 data,” *JCAP*, vol. 1203, p. 030, 2012.

- [40] M. Citron, J. Ellis, F. Luo, J. Marrouche, K. Olive, *et al.*, “The End of the CMSSM Coannihilation Strip is Nigh,” *Phys.Rev.*, vol. D87, p. 036012, 2013.
- [41] D. Ghosh, M. Guchait, S. Raychaudhuri, and D. Sengupta, “How Constrained is the cMSSM?,” *Phys.Rev.*, vol. D86, p. 055007, 2012.
- [42] D. Alves *et al.*, “Simplified Models for LHC New Physics Searches,” *J.Phys.*, vol. G39, p. 105005, 2012.
- [43] J. Alwall, P. Schuster, and N. Toro, “Simplified Models for a First Characterization of New Physics at the LHC,” *Phys.Rev.*, vol. D79, p. 075020, 2009.
- [44] S. Chatrchyan *et al.*, “Interpretation of Searches for Supersymmetry with simplified Models,” *Phys.Rev.*, vol. D88, p. 052017, 2013.
- [45] J. Hisano, K. Kurosawa, and Y. Nomura, “Natural effective supersymmetry,” *Nucl.Phys.*, vol. B584, pp. 3–45, 2000.
- [46] M. Papucci, J. T. Ruderman, and A. Weiler, “Natural SUSY Endures,” *JHEP*, vol. 1209, p. 035, 2012.
- [47] B. Allanach and B. Gripaios, “Hide and Seek With Natural Supersymmetry at the LHC,” *JHEP*, vol. 1205, p. 062, 2012.
- [48] K. Aamodt *et al.*, “The ALICE experiment at the CERN LHC,” *JINST*, vol. 3, p. S08002, 2008.
- [49] G. Aad *et al.*, “The ATLAS Experiment at the CERN Large Hadron Collider,” *JINST*, vol. 3, 2008.
- [50] R. Adolphi *et al.*, “The cms experiment at the cern lhc,” *JINST*, vol. 0803, p. S08004, 2008.
- [51] A. A. Alves *et al.*, “The LHCb Detector at the LHC,” *JINST*, vol. 3, p. S08005, 2008.
- [52] J.-L. Caron, “Lhc layout.. schema general du lhc..” Sep 1997.
- [53] C. Collaboration, “Cms luminosity - public results.” twiki.cern.ch/twiki/bin/view/CMSPublic/LumiPublicResults., 2011.
- [54] CERN, “Cms compact muon solenoid..” <http://public.web.cern.ch/public/Objects/LHC/CMSnc.jpg> Feb 2010.

- 1470 [55] *The CMS electromagnetic calorimeter project: Technical Design Report*. Technical
1471 Design Report CMS, Geneva: CERN, 1997.
- 1472 [56] *The CMS muon project: Technical Design Report*. Technical Design Report CMS,
1473 Geneva: CERN, 1997.
- 1474 [57] CMS Collaboration, “The cms physics technical design report, volume 1,”
1475 *CERN/LHCC*, vol. 2006-001, 2006.
- 1476 [58] M. Cacciari, G. P. Salam, and G. Soyez, “The anti- k_t jet clustering algorithm,”
1477 *Journal of High Energy Physics*, vol. 2008, no. 04, p. 063, 2008.
- 1478 [59] “Jet performance in pp collisions at 7 tev,” Tech. Rep. CMS-PAS-JME-10-003,
1479 CERN, Geneva, 2010.
- 1480 [60] X. Janssen, “Underlying event and jet reconstruction in cms,” Tech. Rep. CMS-CR-
1481 2011-012, CERN, Geneva, Jan 2011.
- 1482 [61] T. C. collaboration, “Determination of jet energy calibration and transverse mo-
1483 mentum resolution in cms,” *Journal of Instrumentation*, vol. 6, no. 11, p. P11002,
1484 2011.
- 1485 [62] R. Eusebi and on behalf of the CMS collaboration), “Jet energy corrections and
1486 uncertainties in cms: reducing their impact on physics measurements,” *Journal of
1487 Physics: Conference Series*, vol. 404, no. 1, p. 012014, 2012.
- 1488 [63] “Algorithms for b Jet identification in CMS,” Tech. Rep. CMS-PAS-BTV-09-001,
1489 CERN, 2009. Geneva, Jul 2009.
- 1490 [64] “Performance of b tagging at $\sqrt{s}=8$ tev in multijet, ttbar and boosted topology
1491 events,” no. CMS-PAS-BTV-13-001, 2013.
- 1492 [65] T. C. collaboration, “Identification of b-quark jets with the cms experiment,” *Journal
1493 of Instrumentation*, vol. 8, no. 04, p. P04013, 2013.
- 1494 [66] S. Dasu *et al.*, “CMS. The TriDAS project. Technical design report, vol. 1: The
1495 trigger systems,” 2000.
- 1496 [67] P. Sphicas, “CMS: The TriDAS project. Technical design report, Vol. 2: Data
1497 acquisition and high-level trigger,” 2002.
- 1498 [68] J. B. et al., “Calibration and Performance of the Jets and Energy Sums in the
1499 Level-1 Trigger ,” no. CMS IN 2013/006 (2013), 2013.

- 1500 [69] B. et al., “Study of Level-1 Trigger Jet Performance in High Pile-up Running
1501 Conditions,” no. CMS IN 2013/007 (2013), 2013.
- 1502 [70] J. J. Brooke, “Performance of the cms level-1 trigger,” Tech. Rep. CMS-CR-2012-322.
1503 CERN-CMS-CR-2012-322, CERN, Geneva, Nov 2012.
- 1504 [71] L. Randall and D. Tucker-Smith, “Dijet searches for supersymmetry at the large
1505 hadron collider,” *Phys. Rev. Lett.*, vol. 101, p. 221803, Nov 2008.
- 1506 [72] “SUSY searches with dijet events,” 2008.
- 1507 [73] “Search strategy for exclusive multi-jet events from supersymmetry at CMS,” Tech.
1508 Rep. CMS-PAS-SUS-09-001, CERN, 2009. Geneva, Jul 2009.
- 1509 [74] “Calorimeter Jet Quality Criteria for the First CMS Collision Data,” Tech. Rep.
1510 CMS-PAS-JME-09-008, CERN, 2010. Geneva, Apr 2010.
- 1511 [75] T. C. collaboration, “Performance of cms muon reconstruction in pp collision events
1512 at $\sqrt{s} = 7$ tev,” *Journal of Instrumentation*, vol. 7, no. 10, p. P10002, 2012.
- 1513 [76] “Search for supersymmetry in events with photons and missing energy,” Tech. Rep.
1514 CMS-PAS-SUS-12-018, CERN, Geneva, 2012.
- 1515 [77] M. Cacciari and G. P. Salam, “Pileup subtraction using jet areas,” *Phys.Lett.*,
1516 vol. B659, pp. 119–126, 2008.
- 1517 [78] Z. Bern, G. Diana, L. J. Dixon, F. Febres Cordero, S. Hoche, H. Ita, D. A. Kosower,
1518 D. Maitre, and K. J. Ozeren, “Driving missing data at next-to-leading order,” *Phys.
1519 Rev. D*, vol. 84, p. 114002, Dec 2011.
- 1520 [79] “Data-Driven Estimation of the Invisible Z Background to the SUSY MET Plus
1521 Jets Search,” Tech. Rep. CMS-PAS-SUS-08-002, CERN, 2009. Geneva, Jan 2009.

1522 Acronyms

1523	ALICE	A Large Ion Collider Experiment
1524	ATLAS	A Toroidal LHC ApparatuS
1525	APD	Avalanche Photo-Diodes
1526	BSM	Beyond Standard Model
1527	CERN	European Organization for Nuclear Research
1528	CMS	Compact Muon Solenoid
1529	CMSSM	Compressed Minimal SuperSymmetric Model
1530	CSC	Cathode Stripe Chamber
1531	CSV	Combined Secondary Vertex
1532	CSVM	Combined Secondary Vertex Medium Working Point
1533	DT	Drift Tube
1534	ECAL	Electromagnetic CALorimeter
1535	EB	Electromagnetic CALorimeter Barrel
1536	EE	Electromagnetic CALorimeter Endcap
1537	ES	Electromagnetic CALorimeter pre-Shower
1538	EMG	Exponentially Modified Gaussian
1539	EPJC	European Physical Journal C
1540	EWK	Electroweak Sector
1541	GCT	Global Calorimeter Trigger
1542	GMT	Global MuonTrigger
1543	GT	Global Trigger
1544	HB	Hadron Barrel
1545	HCAL	Hadronic CALorimeter

1546	HE	Hadron Endcaps
1547	HF	Hadron Forward
1548	HLT	Higher Level Trigger
1549	HO	Hadron Outer
1550	HPD	Hybrid Photo Diode
1551	LUT	Look Up Table
1552	L1	Level 1 Trigger
1553	LHC	Large Hadron Collider
1554	LHCb	Large Hadron Collider Beauty
1555	LSP	Lightest Supersymmetric Partner
1556	POGs	Physics Object Groups
1557	PS	Proton Synchrotron
1558	QED	Quantum Electro-Dynamics
1559	QCD	Quantum Chromo-Dynamics
1560	QFT	Quantum Field Theory
1561	RPC	Resistive Plate Chamber
1562	RCT	Regional Calorimeter Trigger
1563	RMT	Regional Muon Trigger
1564	SUSY	SUperSYmmetry
1565	SM	Standard Model
1566	SMS	Simplified Model Spectra
1567	SPS	Super Proton Synchrotron
1568	TF	Transfer Factor
1569	VEV	Vacuum Expectation Value
1570	VPT	Vacuum Photo-Triodes

₁₅₇₁ **WIMP** Weakly Interacting Massive Particle